Sebastian J. Mühlbauer

Multiscale modeling of heterogeneous catalysis in porous metal foam structures using particle-based simulation methods

FAU
UNIVERSITY PRESS

Sebastian J. Mühlbauer

Multiscale modeling of heterogeneous catalysis in porous metal foam structures using particle-based simulation methods

FAU Forschungen, Reihe B

Medizin, Naturwissenschaft, Technik

Band 30

Sebastian J. Mühlbauer

Multiscale modeling of heterogeneous catalysis in porous metal foam structures using particle-based simulation methods

Multiscale modeling of
heterogeneous catalysis in porous metal foam structures
using particle-based simulation methods

Multiskalenmodellierung
heterogener Katalyse in porösen Metallschäumen
mithilfe partikelbasierter Simulationsmethoden

Der Technischen Fakultät

der Friedrich-Alexander-Universität

Erlangen-Nürnberg

zur
Erlangung des Doktorgrades Dr.-Ing.

vorgelegt von

Sebastian Josef Mühlbauer

aus Viechtach

Abstract

Heterogeneous catalysis is omnipresent in the chemical industry. In contrast to homogeneous catalysis, no expensive separation processes have to be performed subsequently. Conversely, the challenge is to ensure fast mass transfer between the fluid phase and the reactive surface. In this context, porous foams are an extremely promising support structure. The scope of this work is to investigate and optimize heterogeneous catalysis in porous metal foam structures on two different size scales.

First, we consider the gas dynamics together with the reaction and diffusion processes in individual foam pores on the mesoscale. To this end, the unit foam cell is defined as an inverse sphere packing, and described using Constructive Solid Geometry. In order to eliminate numerical artifacts at the complex shaped boundary, we construct an isotropic version of the mesoscopic simulation method, Stochastic Rotation Dynamics. Further, we develop specialized boundary conditions to model open boundaries in particle-based simulations of reactive flow. Within the scope of this work, the foam structures are assumed to be coated with an even washcoat layer. The washcoat is not simulated explicitly. Instead, the effective reaction rate is determined based on the previously tabulated effectiveness factor for the washcoat. On the basis of experimental results, the implemented simulation model is validated regarding permeability and mass transport towards the reactive surface. As prototype reaction we consider the low temperature water-gas shift. The trade-off between chemical conversion and flow resistance is characterized by the performance index. In search of favorable process parameters, which lead to a high performance index, the porosity is varied. The effective reaction rate can be varied by adjusting the active site density in the washcoat layer. Herby, both the mass transfer limited, and the reaction rate limited regime can be assessed. In the mass transfer limited regime, we observe that increasing the porosity improves the performance index. This observation coincides with findings from the literature. Moreover, the reactive surface is utilized more efficiently at larger porosity values. As the effective reaction rate in the washcoat is

decreased, the system is shifted towards the reaction rate limited regime, and the correlations between porosity and performance index as well as surface exploitation are less pronounced.

Second, we condense the detailed simulation results on the mesoscale to relations between few dimensionless numbers. Based on these relations, we follow a multiscale approach to derive an efficient, one-dimensional, macroscale model for heterogeneous catalysis in open-cell porous metal foam. Due to its industrial importance, we focus on the mass transfer limited regime. For the fixed foam porosity 0.902, we find the most favorable ratio between conversion and flow resistance to be achieved at the Reynolds number 15.8.

Additionally, we present simple recipes to determine the optimum configuration for metal foam filled catalytic converters under different circumstances. In case the reaction heat is negligible, the optimum performance is reached using one single foam segment the pore size of which is adjusted such that the optimum Reynolds number is obtained. However, for realistic heat release values, the heat transfer out of the catalytic converter is critical. In order to keep temperature fluctuations small, under these circumstances, the optimum configuration consists of several, stacked foam segments with decreasing pore size along the main flow direction. For this case, we provide an analytical procedure to determine the optimum pore size for each of the stacked segments. Demanding the chemical conversion to be $99.5\,\%$, we compare the optimized configuration to the reference configuration with constant pore size for typical parameters. We observe that, compared to this reference, the performance index can be increased by up to $11.0\,\%$, and the required reactive surface area, i.e., the amount of catalytic material, can be reduced by up to $18.4\,\%$.

Zusammenfassung

Heterogene Katalyse ist allgegenwärtig in der chemischen Industrie. Verglichen mit homogener Katalyse hat dieses Verfahren den Vorteil, dass keine aufwendigen Trennprozesse nachgeschaltet werden müssen. Im Gegenzug liegt die Herausforderung darin einen schnellen Stofftransport zwischen der Fluidphase und der reaktiven Oberfläche zu gewährleisten. Vor diesem Hintergrund stellen poröse Schaumstrukturen eine äußerst vielversprechende Trägerstruktur dar. Diese Arbeit befasst sich mit der Untersuchung und Optimierung heterogener Katalyse in porösen Metallschaumstrukturen auf zwei verschiedenen Größenskalen.

Zunächst betrachten wir die Strömungsverhältnisse sowie die Reaktions- und Diffusionsprozesse innerhalb einer einzelnen Schaumpore auf Mesoskala. Wir definieren dazu eine Einheitsschaumzelle als Packung inverser Kugeln, die sich mithilfe von Constructive Solid Geometry beschreiben lässt. Um numerische Artefakte an den komplex geformten Rändern zu vermeiden, konstruieren wir eine isotrope Variante der mesoskopischen Simulationsmethode Stochastic Rotation Dynamics. Darüber hinaus entwickeln wir eine spezielle Randbedingung zur Beschreibung offener Ränder in partikelbasierten Simulationen von reaktiven Strömungen. Im Rahmen dieser Arbeit, nehmen wir an, dass die Schaumstruktur gleichmäßig mit Washcoat beschichtet ist. Der Washcoat wird nicht explizit simuliert. Stattdessen wird basierend auf dem zuvor tabellierten Katalysatorwirkungsgrad im Washcoat eine effektive Reaktionsrate bestimmt. Anhand von experimentellen Ergebnissen wird das implementierte Simulationsmodell im Hinblick auf die Permeabilität und den Stofftransport hin zur reaktiven Oberfläche validiert. Als Prototypreaktion wählen wir den Niedertemperatur-Wasser-Gas-Shift. Das Verhältnis zwischen chemischer Umwandlung und Strömungswiderstand wird durch den Performance Index charakterisiert. Auf der Suche nach günstigen Prozessparametern, die zu einem hohen Performance Index führen, variieren wir die Schaumporosität. Die effektive Reaktionsrate innerhalb der Washcoatschicht kann durch Änderung der Dichte der aktiven Zentren eingestellt werden. Auf diese Weise kann sowohl

das durch den Stofftransport limitierte, als auch das durch die Reaktionsrate limitierte Regime untersucht werden. In dem durch den Stofftransport limitierten Regime ist zu beobachten, dass bei einer Erhöhung der Porosität auch der Performance Index ansteigt. Dies steht im Einklang mit der Literatur. Darüber hinaus wird die reaktive Oberfläche bei größeren Porositätswerten effizienter genutzt. Bei einer Verringerung der effektiven Reaktionsrate innerhalb der Washcoatschicht verschiebt sich das System in Richtung des durch die Reaktionsrate limitierten Regimes und die Korrelationen zwischen Porosität und Performance Index sowie Oberflächennutzung sind weniger ausgeprägt.

Im Anschluss daran, kondensieren wir die detaillierten Simulationsergebnisse auf Mesoskala zu Zusammenhängen zwischen wenigen, dimensionslosen Kennzahlen. Darauf aufbauend wenden wir einen Multiskalenansatz an, um ein effizientes, eindimensionales, makroskopisches Modell zur Beschreibung heterogener Katalyse in offenporigen, porösen, Metallschäumen abzuleiten. Aufgrund dessen industrieller Bedeutung konzentrieren wir uns in diesem Schritt auf das Regime, in dem der Stofftransport den limitierenden Faktor darstellt. Für eine konstante Schaumporosität von $0,902$ beobachten wir, dass das günstigste Verhältnis zwischen chemischer Umwandlung und Strömungswiderstand, bei einer Reynolds-Zahl von $15,8$ erreicht wird.

Darüber hinaus erstellen wir einfache Anleitungen, um die optimale Konfiguration für mit Metallschaum gefüllte Katalysatoren unter verschiedenen Bedingungen zu bestimmen. Ist die Reaktionswärme vernachlässigbar, so liefert ein einzelnes Schaumsegment die optimale Leistung, dessen Porengröße so gewählt ist, dass die optimale Reynolds-Zahl erreicht wird. Für realistische Werte der Reaktionswärme ist jedoch die Wärmeableitung aus dem Katalysator entscheidend. Um Temperaturschwankungen gering zu halten, besteht die optimale Konfiguration in diesem Fall aus mehreren, aneinandergereihten Schaumsegmenten mit abnehmender Porengröße entlang der Hauptströmungsrichtung. Für diesen Fall präsentieren wir ein analytisches Verfahren, um die optimale Porengröße für jedes der aneinandergereihten Segmente zu bestimmen. Für typische Parameter und eine geforderte chemische Umwandlung von $99,5\%$ stellen wir die optimierte Konfiguration der Referenzkonfiguration mit konstanter Porengröße gegenüber. Im Vergleich zu dieser Referenzkonfiguration kann der Performance Index um bis zu $11,0\%$ und die erforderliche reaktive Oberfläche, d.h. die Menge an katalytischem Material, um bis zu $18,4\%$ reduziert werden.

Acknowledgments

First and foremost, I would like to thank my supervisor, Prof. Thorsten Pöschel, supporting and encouraging me throughout the project. While guiding me with valuable remarks and suggestions, he has still given me the freedom to discover and explore the various fascinating aspects of the subject independently. Furthermore, I would like to thank Dr. Severin Strobl, who has not only provided the simulation software which has been the basis for my numerical investigations, but also valuable advice for extending this software in order to meet my needs. I would like to thank Severin and all my colleagues at the MSS for the countless inspiring scientific discussions and, in particular, for the amicable working atmosphere.

I owe many thanks to my close friends and, especially, to my family for their continual support throughout my studies. Without my parents' lifelong support, I would have not been able to reach this point. Finally, I would like to thank my girlfriend, Julia, whose continual encouragement allowed me to bring this project to a successful conclusion.

Contents

1 Introduction

1.1 Motivation

Many industrial chemical processes require catalysts. Hence, understanding and optimizing catalytic processes is of great economical importance [1]. In homogeneous catalysis, the catalyst and the reactants are present in the same fluid phase. Subsequent to the actual reaction, separation processes are necessary to retrieve the products. Conversely, in heterogeneous catalysis, the catalyst is applied to a solid support structure, and the critical step typically is to bring the reactants to the catalyst. Heterogeneous catalysis is particularly suitable for continuous reactors, since the catalyst remains on the support structure, while the products can be led to the next process step. In order to provide a large interface between the support structure and the fluid phase, porous structures, such as washcoated monoliths or pellet packings, are preferred [2, 3]. An important challenge in reactor design is to find support structures which ensure an effective mass transport to the surface, while avoiding large pressure drops. In this context, open-cell foam structures are extremely promising [4]. Due to high porosity, specific surface and tortuosity, these structures provide excellent mass transport properties at moderate pressure drops [5]. Therefore, their performance in heterogeneous catalysis has been investigated experimentally [6, 7, 8] as well as numerically for regular [9, 10] and irregular structures [11, 5]. In these studies, the foam structures are modeled as Kelvin cells[1], and continuum approaches – like the finite volume method – are used to solve for the concentration and flow fields. In this framework, complex geometries can be treated with an accordingly shaped mesh or using immersed boundaries [12]. For both cases, the accuracy of the boundary description depends on the spacial discretization.

In this thesis, we follow a different approach. Instead of continuum methods, we use a mesoscopic, particle-based method to simulate the

---

[1] A sketch of this structure is provided in [11].
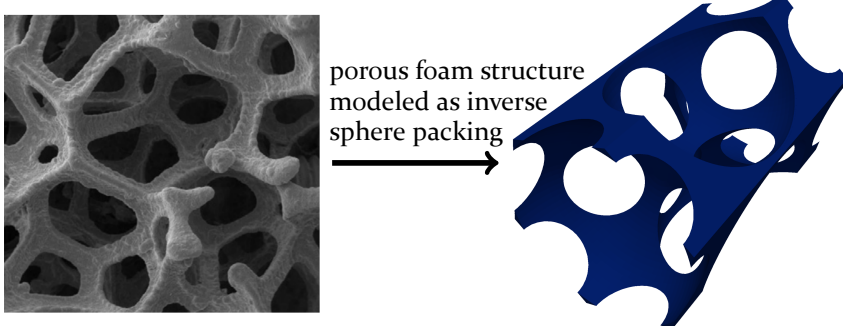
processes within individual foam pores. Mesoscale simulation techniques bridge the gap between molecular scale and continuum approaches on the macroscopic scale [13]. The unit foam cell, which is depicted in Fig. 1.1, is modeled as an inverse sphere packing and described with Constructive Solid Geometry (CSG) [14, 15]. This combination allows for an easy handling of the chemical reactions at the foam surface. Moreover, for the employed meso-scopic simulation method, a phenomenological description is sufficient, i.e, no partial differential equations are required to describe the system. Conversely, applied to macroscopic systems, mesoscale simulation methods often are numerically more expensive than continuum methods.

The final aim of this work is to optimize the design of metal foam reactors on the macroscale with the local pore size as free parameter. To address this problem, the macroscopic catalytic converter must be assessed for numerous different pore size configurations, which is feasible neither in an experimental study nor by means of direct numerical simulations. Therefore, based on the simulation results gathered on the mesoscale, we follow a multiscale approach to develop an efficient model for the simulation of catalytic converters on the macroscale.

1.2 Thesis outline

In this thesis, we develop a multiscale approach to predict the processes within catalytic converters on the macroscale based on detailed simulation results for representative foam cells on the mesoscale. The transition between the different scales is achieved by using dimensionless numbers to characterize the system. In the macroscale simulations, the local reactant conversion as well as the local pressure drop are needed as input. In order to predict the conversion on the macroscale, we establish a relation between Sherwood number and Reynolds number in metal foam structures on the mesoscale. Conversely, for the pressure drop, depending on foam porosity, we determine the relation between Hagen number and Reynolds number. Subsequently, using homogenization, we develop an efficient, one-dimensional model for macroscale simulations of catalytic converters filled with washcoated metal foam. Finally, this model is applied to determine the optimum configuration for heterogeneous catalysis in porous foam structures.

As shown in Fig. 1.1, the foam structure is modeled as an inverse sphere packing. Strobl has developed a numerical framework for particle-based gas dynamics simulations in complex geometries, described by Constructive

porous foam structure
modeled as inverse
sphere packing

FIG. 1.1: The open-cell metal foam structure[2] depicted on the left is modeled as an inverse sphere packing. The representative unit foam cell employed on the mesoscale is shown on the right.

Solid Geometry (CSG) [13, 15]. Hence, the simulation domain is defined analytically, which has the advantage that the chemical reactions can be performed exactly at the reactive surface independently of the spacial resolution of the domain. In the framework developed by Strobl, the gas phase is modeled using Direct Simulation Monte Carlo (DSMC) [16]. Being the direct implementation of the Boltzmann equation, this model is well established. Before being capable of performing the numerical simulations on the mesoscale which are required for the proposed multiscale approach, this simulation software has to be extended by the following *three essential ingredients*:

Efficient isotropic gas dynamics model. The computational cost associated with DSMC is proportional to the particle collision rate, i.e., this method is especially suitable for rarefied gas dynamics [17]. For denser systems, Stochastic Rotation dynamics (SRD) [18] is better suited, since it applies an effective multi-particle collision instead of binary collisions. In its standard form, SRD groups the particles into Cartesian grid cells, and the particles exchange momentum only within these cells. This may introduce artificial anisotropy in the vicinity of complex shaped walls. In order to eliminate such artifacts, an isotropic version of Stochastic Rotation dynamics is developed in Chap. 2.

---

[2] Reprinted from *Acta Materialia*, 59, O. Smorygo, V. Mikutski, A. Marukovich, A. Ilyushchanka, V. Sadykov, and A. Smirnova, An inverted spherical model of an open-cell foam structure, 2671, Copyright 2011, with permission from Elsevier.

Boundary condition for inlet and outlet. Concerning particle-based methods, Neumann boundary conditions tend to suffer from instabilities [19]. Simple periodic boundary conditions are not applicable in this case, since the reactant concentrations at inlet and outlet differ, due to the chemical reactions in the domain. To circumvent this problem, we connect inlet and outlet via a modified periodic boundary condition allowing for discontinuities in the concentration field, while the density, temperature and the velocity fields are strictly periodic. In order to drive the flow, an external acceleration is applied. Note that these specialized inlet and outlet boundary conditions are applicable only to volume conserving reactions. A detailed description is provided in Chap. 3.

Boundary condition for heterogeneous catalysis. We are considering the low temperature water-gas shift as prototype reaction. Hence, we implement the catalytic boundary conditions explicitly for the low temperature water-gas shift reaction, see Sec. 4.2. We assume the reaction to follow the Langmuir-Hinshelwood reaction mechanism [20, 21]. The foam structure serves as substrate and is assumed to be coated with $CuO/ZnO/Al_2O_3$ washcoat. As we do not restrict this study to the mass transfer limited regime, but also consider the reaction rate limited regime, it is eminently important to model the reaction mechanism in detail. The effective reaction rate in the washcoat layer is computed using precomputed look-up tables for the effectiveness factor [22]. Among other parameters, the effective reaction rate depends on the partial surface pressures of the reactants, which can be computed from the collision fluxes on the surface. Hence, the relevant quantities are evaluated directly at the reactive boundary.

The implemented model is capable of simulating gas dynamics superimposed by reaction and diffusion processes in complex shaped domains. In Sec. 4.3, the simulation model is validated for the representative unit cell against experimental findings for both the pressure drop [23] and the conversion [6] in metal foam structures. In Sec. 4.4.2, we apply the validated model to representative unit foam cells and assess the trade-off between conversion and flow resistance as a function of porosity. This porosity study is not restricted to the mass transfer limited regime, but we consider also an intermediate regime as well as the reaction rate limited regime.

Relations between Sherwood and Reynolds number as well as Hagen and Reynolds number are determined for the representative unit foam cell in Sec. 4.3 and Sec. 5.3. In the macroscale simulation, described in Sec. 5.2, we assume the mass transfer to be the limiting step. The foam structure is modeled as homogeneous continuum with freely definable pore size profile.

For the local pore size, the local Reynolds number and, consequently, the local Sherwood and Hagen number can be determined. Subsequently, conversion and pressure drop along the catalytic converter can be determined based on local Sherwood and Hagen number, respectively. In Sec. 5.3, we use the macroscale model to examine two different scenarios: negligible and realistic heat of reaction. For each scenario, we present a simple recipe to find an optimum pore size profile along the catalytic converter.

2 Isotropic Stochastic Rotation Dynamics[1]

"Stochastic Rotation Dynamics (SRD) is a widely used method for the mesoscopic modeling of complex fluids, such as colloidal suspensions, or multiphase flows. In this method, however, the underlying Cartesian grid defining the coarse-grained interaction volumes induces anisotropy. We propose an isotropic, lattice-free variant of [Stochastic Rotation Dynamics], termed iSRD. Instead of Cartesian grid cells, we employ randomly distributed spherical interaction volumes. This eliminates the requirement of a grid-shift, which is essential in standard SRD to maintain Galilean invariance. We derive analytical expressions for the viscosity and the diffusion coefficient in relation to the model parameters, which show excellent agreement with the results obtained in iSRD simulations. The proposed algorithm is particularly suitable to model systems bound by walls of complex shape, where the domain cannot be meshed uniformly. The presented approach is not limited to SRD, but is applicable to any other mesoscopic method, where particles interact within certain coarse-grained volumes.

2.1 Introduction

During the last years particle-based fluid simulation methods have been well established as an alternative to continuum methods. They have important advantages, especially in situations where the continuum assumption does not hold, but also for complex fluids, such as colloidal suspensions, or multiphase flows [25, 26, 27, 28, 29]. With molecular dynamics, for example, complex fluids can be simulated on the molecular level including the actual microscopic interaction laws [30]. In contrast, the particles employed in Direct Simulation Monte Carlo (DSMC) [16] do not represent physical particles, but rather probability quanta, composing the velocity distribution

---

function. In DSMC, the particle trajectories are not computed deterministically, as in molecular dynamics. Instead, binary collisions are performed to model the transport of momentum, and eventually solve the nonlinear Boltzmann equation [31]. Thus, unlike computational fluid dynamics (CFD), based on the numerical solution of hydrodynamic equations, DSMC does not rely on relations between the hydrodynamic fields, and is also reliable in cases where the hydrodynamic description of the system is problematic, for instance in the presence of shocks [32]. Further important fields of application are flows at moderate to high Knudsen number, such as rarefied gases [17], flows in the vicinity of boundaries [33], or flows in microfluidic devices [34], where the mean free path does not fulfill the condition of being much smaller than the system dimensions. In most cases, DSMC consumes significantly larger computational resources than field-based CFD. In return, it has a wider range of validity than CDF, since DSMC relies exclusively on the validity of the Boltzmann description. Still, there are also cases where this simulation method is computationally efficient, e.g., for rarefied gas flows with a large mean free path, and rather few particle collisions, since the computational cost of DSMC is proportional to the particle collision rate.

For application to denser gases, however, Stochastic Rotation Dynamics (SRD), developed by Malevanets and Kapral [18], is more efficient, compromising between DSMC and CFD: Instead of numerous binary collision, one so-called multi-particle collision is performed to exchange momentum between all particles within certain coarse-graining volumes, which usually are the cells of a Cartesian grid spanning the simulation volume. The size as well as the shape of the coarse-graining volumes has significant influence on the transport coefficients. Therefore, a grid composed of cubic cells is used for the majority of applications. In order to model complicated domains, an additional surface grid, describing the boundaries, has to be embedded into the regular simulation grid. It was shown that in its basic form, SRD does not preserve Galilean invariance, which can be corrected by a random *grid-shift*, that is, the simulation grid has to be shifted randomly before each collision step [35]. The grid-shift assures Galilean invariance, however, it does not correct the anisotropy caused by the underlying cubic grid [36]. Ihle et al. [36] conjectured that additional random grid rotations would restore isotropy in SRD.

For the case of DSMC, which suffers from similar problems, in order to achieve isotropy, Donev et al. [37] suggest a grid-free version, termed isotropic DSMC (iDSMC). While in standard DSMC only particles from the same grid cell are allowed to collide, in iDSMC random particle pairs

are chosen to transfer momentum, if they are not further apart than a given distance, disregarding their cell affiliation. This procedure leads to an isotropic interaction between the quasi-particles [37, 38].

Following a similar idea, we propose a grid-free, truly Lagrangian version of SRD which we call *isotropic Stochastic Rotation Dynamics* (iSRD).

We will first provide a short review of SRD and the corresponding relations for the transport coefficients. Subsequently, we will describe our approach to eliminate the influence of the spatial discretization, and derive analytical expressions for the viscosity and the diffusion coefficient in this case. Finally, we compare these expressions with measurements of the transport coefficients obtained from simulations.

2.2   **Stochastic Rotation Dynamics**

SRD is a Lagrangian approach, where the fluid is represented by particles. Each time step of the simulation, Δt, comprises a streaming and a collision step. The streaming step propagates the particles according to their current velocity,

$$\vec{r}_i(t + \Delta t) = \vec{r}_i(t) + \Delta t\, \vec{v}_i(t)\,, \tag{2.1}$$
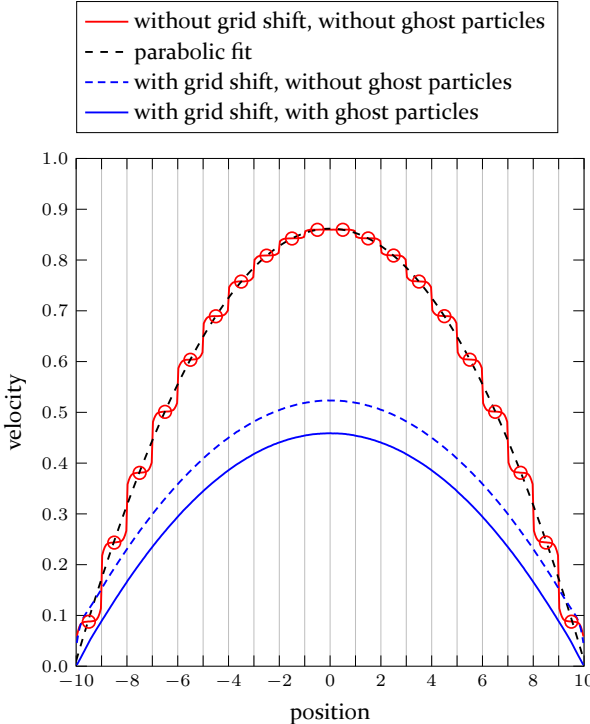
where $\vec{r}_i$ and $\vec{v}_i$ denote the position and velocity of particle i, respectively. The collision step randomly rotates the fluctuating contribution to the particles' velocities, which is related to the temperature of the fluid, according to the collision rule

$$\vec{v}_i(t + \Delta t) = \vec{u}(t)|_i + \hat{R}\cdot \left[\vec{v}_i(t) - \vec{u}(t)|_i\right]\,, \tag{2.2}$$

where $\vec{u}(t)$ is the macroscopic flow velocity field and $\vec{u}(t)|_i$ is the value of the field at the location of particle i. In SRD, the field $\vec{u}$ is obtained by coarse-graining the velocities of all particles of the system, using a Cartesian grid spanning the simulation domain. Thus, the flow velocity corresponding to the ith particle is estimated as the mean velocity of all particles residing in the same grid cell, C, as $\vec{u}(t)|_i \equiv \langle\vec{v}\rangle^C$, and the particle's thermal velocity is $\left[\vec{v}_i(t) - \langle\vec{v}\rangle^C\right]$. In three-dimensional simulations, the rotation matrix, $\hat{R}$, represents a rotation by a constant rotation angle, α, where the rotation axis is randomly chosen in each collision step for each grid cell [18, 25].

As an example and for later reference, in Fig. 2.1 we present the flow profile for plane Poiseuille flow with simple bounce-back boundary conditions [39] at the walls and periodic boundaries in the other two spatial directions. The SRD implementation used is built on the framework developed by Strobl [13].

If not specified otherwise, here and in the following we use dimensionless parameters, that is, the cell width, $a = 1$, time step, $\Delta t = 0.1$, thermal velocity, $\sqrt{kT/m} = 1$, and the rotation angle $\alpha = \pi/2$. The number of particles is chosen such that on average $M = 10$ particles reside in each grid cell. The flow is driven by an external acceleration of 5×10^{-3}. Temperature is kept constant by means of the cell-level thermostat which was developed by Hecht et al. [40, 41] based on Refs. [42, 43]. To obtain

FIG. 2.1: The upper curves correspond to plane Poiseuille flow simulated using SRD without grid-shift. The discretization of the channel, which is 20 cells wide, is shown by the vertical thin lines. The particle velocities are averaged within slices oriented parallel to the channel walls. The symbols (○) show the average particle velocity within slices having width a. The upper dashed line is a parabola fitted to this averaged velocity profile in the interval $[-5, 5]$, i.e., distant from the walls. The red solid line represents the detailed flow profile, obtained by averaging within slices of width $a/20$. The two lower curves show the results for SRD with grid-shift, using the same parameters as before. To reduce velocity slip at the walls, for the solid blue line, ghost particles (see Sec. 2.5.5) were used in addition to the grid-shift.

the flow profile shown in Fig. 2.1, we average the particle velocities within slices parallel to the channel walls, considering two different slice widths. For the symbols (○), the slice width is chosen to be equal to the cell width,

a. These cell averaged velocities agree very well with the fitted parabola drawn as a dashed line. Considering, however, the solid line representing the finer resolved flow profile, which is obtained by averaging within slices having a width of $a/20$, we perceive distinct steps, connecting the plateaus within the simulation cells. This effect reveals a violation of the molecular chaos assumption: In case the mean free path is small compared to the cell width, many particles remain in one grid cell for several time steps, colliding with each other repeatedly and, thus, correlating the velocities of the particles in the same cell. To reduce pre-collisional correlations, and to make SRD Galilean-invariant, the so-called grid-shift [35, 25] can be applied: Before each collision step the simulation grid is shifted by a random vector $\vec{s} = [s_x, s_y, s_z]$, with $s_x, s_y, s_z \in [-a/2, a/2]$. This procedure is sensible, only as long as the simulation domain is discretized using a regular cubic grid. For the setup from Fig. 2.1, the grid-shift enhances the transport of momentum across the channel, i.e., the shear viscosity [44]. Activating the grid-shift leads to smooth velocity profiles: The solid and dashed blue lines represent the corresponding simulation results with and without ghost particles, as introduced in Sec. 2.5.5, respectively.

2.3 Transport Coefficients in SRD

As pointed out in Ref. [25], different approaches have been applied to characterize the SRD fluid. While in some works [36, 45, 46, 44, 47] the transport coefficients are investigated based on equilibrium calculations, other authors consider the system's response to imposed non-equilibrium conditions [48, 49]. Both approaches lead to identical results for the transport coefficients. The viscosity of a fluid simulated with SRD is known to have two contributions, which are denoted as the *kinetic* and the *collisional* part [50]. Under the assumption of molecular chaos, Kikuchi et al. [48] derive analytical expressions for these two contributions. Considering stationary Couette flow with the flow profile $\vec{u}(y) = [\dot{\gamma}\, y, 0, 0]$, where the shear rate, $\dot{\gamma} \equiv \partial u_x(y)/\partial y$, is constant, Kikuchi et al. find for the kinetic contribution to the viscosity in the three-dimensional case:

$$\nu_{\mathrm{SRD}}^{\mathrm{kin}} = \frac{k_B\, T}{m}\Delta t \left(\frac{1}{2} + \frac{f}{1 - f} \right), \qquad (2.3)$$

where k_B, T and m denote the Boltzmann constant, the temperature and the particle mass, respectively. The term

$$f(\alpha, n) = 1 - \left(\frac{n-1}{n} \right) \frac{2}{5}\, (2 - \cos\alpha - \cos 2\alpha) \qquad (2.4)$$

describes the relative change in the correlation $\langle v_x\, v_y\rangle$ due to the collision operator from Eq. (2.2) in case exactly n particles are contained in the considered grid cell,

$$\langle v_x(t+\Delta t)\, v_y(t+\Delta t)\rangle = f(\alpha, n)\, \langle v_x(t)\, v_y(t)\rangle\ . \tag{2.5}$$

However, the number of particles, n, contained in the collision cells is not constant but Poisson distributed. Averaging over $n \in \{1, 2, ..., \infty\}$ yields

$$f(\alpha, M) = 1 - \frac{M - 1 + e^{-M}}{M}\frac{2}{5}\left(2 - \cos\alpha - \cos 2\alpha\right) \tag{2.6}$$

and

$$\langle v_x(t+\Delta t)\, v_y(t+\Delta t)\rangle = f(\alpha, M)\, \langle v_x(t)\, v_y(t)\rangle\ , \tag{2.7}$$

with M being the average number of particles per cell. An analogous procedure leads to an analytical expression for the diffusion coefficient, having no collisional contribution [25],

$$D_{\text{SRD}} = \frac{k_B\, T}{m}\Delta t\left(\frac{1}{2} + \frac{g}{1-g}\right)\ , \tag{2.8}$$

where

$$g(\alpha, M) = 1 - \frac{M - 1 + e^{-M}}{M}\frac{2}{3}\left(1 - \cos\alpha\right)\ . \tag{2.9}$$
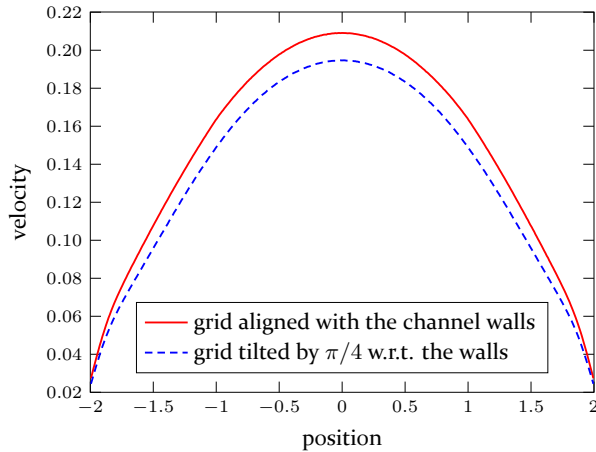
In order to obtain the collisional part of the viscosity, Kikuchi et al. [48] compute the momentum exchange along the direction of the velocity gradient due to the collision step for the considered Couette flow and obtain

$$\nu_{\text{SRD}}^{\text{coll}} = \frac{a^2}{18\,\Delta t}\frac{M - 1 + e^{-M}}{M}\left(1 - \cos\alpha\right)\ . \tag{2.10}$$

For the derivation of Eq. (2.10), the flow profile is required to be smooth, which can be accomplished by the use of a grid-shift, as shown in Fig. 2.1. The results for the kinetic part of the viscosity, Eq. (2.3) together with Eq. (2.6), as well as for the collisional contribution, Eq. (2.10), match the corresponding simulation results [48].

2.4 Effect of grid orientation in SRD

As pointed out by Ihle et al. [36], the underlying cubic grid leads to anisotropy in standard SRD. Concerning the SRD fluid in the bulk, in most practical applications, this anisotropy has only minor influence on the result.

FIG. 2.2: Plane Poiseuille flow simulated using SRD with grid-shift and two different grid orientations. The channel walls are modeled following the approach described in [39].

In the vicinity of walls, however, the interplay between grid orientation and boundary condition can indeed affect the simulation result. To illustrate this issue, plane Poiseuille flow in a comparatively narrow channel is simulated. The flow is driven by an external acceleration of 5×10^{-2}. All other simulation parameters are equal to those from Sec. 2.2. The channel walls are modeled as bounce-back boundary conditions combined with the commonly used ghost particles proposed in [39]. The solid line in Fig. 2.2 represents the velocity profile obtained when the grid is exactly aligned with the channel walls. In contrast, after the grid being rotated by $\pi/4$ with respect to the channel walls, identical simulation parameters lead to the dashed curve. The discrepancy between the two curves demonstrates that, depending on the implemented boundary conditions, the grid orientation can have significant influence on the resulting flow field.

2.5 Isotropic SRD

2.5.1 Description of the method

In standard SRD, even with grid-shift, the underlying Cartesian simulation grid induces anisotropy, as shown in the previous section. Using isotropic coarse-graining volumes, this problem can be eliminated in a natural way, and without the necessity of performing random grid-rotations [36] to correct for the anisotropy introduced by the lattice. Instead of using cubic

lattice cells for coarse-graining, we suggest to use spheres of constant size, which are randomly distributed over the simulation domain. Consequently, the local mean velocity needed for the collision step (see Eq. (2.2)) is now evaluated by averaging the velocities of the particles residing in the same sphere, S, that is, $\vec{u}(t)|_i \equiv \langle \vec{v} \rangle^S$, and the thermal velocity of the ith particle is $\left[\vec{v}_i - \langle \vec{v} \rangle^S \right]$.

Note that this approach is grid-free. For computational efficiency we use an auxiliary grid to sort the particles into the coarse-graining spheres. This grid is not necessarily Cartesian but can be chosen irregular, such that the union of all grid cells covers the simulation domain. Unlike for standard SRD, this grid does, however, not affect the simulation results, as we will demonstrate in Sec. 2.5.6. In analogy to isotropic DSMC [37, 38] we refer to this method as *isotropic SRD* (iSRD).

2.5.2 Definition of the coarse-graining volumes

In standard SRD with grid-shift, the coarse-graining volumes are the cubic cells of a Cartesian grid with a number of basic properties:

  i. The coarse-graining volumes are homogeneously distributed in physical space.

 ii. The total number of coarse-graining volumes is given by the ratio between domain volume and coarse-graining volume. It is, therefore, invariant in time.

iii. At any time, each particle resides in exactly one coarse-graining volume.

We will see that in iSRD these properties do not hold true strictly, but only in a statistical sense. It will be shown, however, that the obtained simulation data agree well with analytical results.

In difference to standard SRD, in iSRD the location of each (spherical) coarse-graining volume is determined randomly. The centers of the coarse-graining spheres shall be uniformly distributed in the simulation domain, however, each unit of physical space contains the same number of coarse-graining spheres only on average. Note that the randomness in the sphere positions has a similar effect as the grid-shift in SRD. It reduces pre-collisional correlations and ensures Galilean invariance.

Sorting the SRD particles into the coarse-graining spheres is a computationally expensive process, as it has to be repeated in each time step.

Therefore, we suggest to employ an auxiliary grid. In Sec. 2.5.6 we will show that this auxiliary grid, while significantly enhancing the efficiency of the simulation, does not affect the simulation result.

The number of coarse-graining spheres, k_l, within cell l of the auxiliary mesh is a Poisson distributed random number with probability density

$$P_{\Lambda_l}(k_l) = \frac{\Lambda_l^{k_l}}{k_l!} e^{-\Lambda_l} . \tag{2.11}$$

In the simulation, we first determine the number of coarse-graining spheres in the lth cell according to the distribution P_{Λ_l}, Eq. (2.11), and then choose the locations of the sphere centers randomly inside the cell. Since particles can be located in more than one coarse-graining volume, they can take part in more than one multi-particle collision per time step. In order to avoid any systematic effect, overlapping coarse-graining spheres should be processed in random order.

The distribution of coarse-graining volumes shall be homogeneous over the domain (*i.*), that is, independent of the cell volume, V_l^C. Therefore, for two arbitrary cells l and l',

$$\frac{\Lambda_l}{\Lambda_{l'}} = \frac{V_l^C}{V_{l'}^C} , \tag{2.12}$$

that is, the expectation values for the number of coarse-graining volumes in a cell relate as the cell volumes. Together with the normalization condition

$$\sum_l V_l^C = \sum_l \Lambda_l V^S \tag{2.13}$$

we obtain

$$\Lambda_l = \frac{V_l^C}{V^S} , \tag{2.14}$$

where V^S is the volume of a coarse-graining sphere. Summing over all cells and denoting the volume of the entire domain by V, we obtain

$$\Lambda \equiv \sum_l \Lambda_l = V/V^S \tag{2.15}$$

and, thus, the expectation value for the total number of coarse-graining spheres in a given volume, V, does not depend on the auxiliary grid, that is, (*ii.*) is statistically fulfilled.

Let us finally consider property (*iii.*): The probability that a particle is located in a randomly placed coarse-graining sphere of volume V^S is given by

the ratio $V^S/V = 1/\Lambda$, where V is the total volume of the domain. Assume, N coarse-graining spheres are placed randomly and independently in the domain. The probability, A_j, for a certain particle to be simultaneously located in exactly j coarse-graining spheres then obeys a binomial distribution

$$A_j = B\left(j\,|N,\,1/\Lambda\right) \approx B\left(j\,|\Lambda,\,1/\Lambda\right)\,, \tag{2.16}$$

where the expectation value for N is given in Eq. (2.15). Albeit the total number of coarse-graining spheres is a fluctuating quantity, for the majority of applications the domain volume is much larger than the coarse-graining volume and, therefore, $\Lambda \gg 1$, implying that the relative fluctuations, $\Delta N/N \approx 1/\sqrt{\Lambda}$, are small. We can further exploit the convergence of the binomial distribution to a Poisson distribution, leading to

$$A_j \approx \frac{e^{-1}}{j!}\,. \tag{2.17}$$
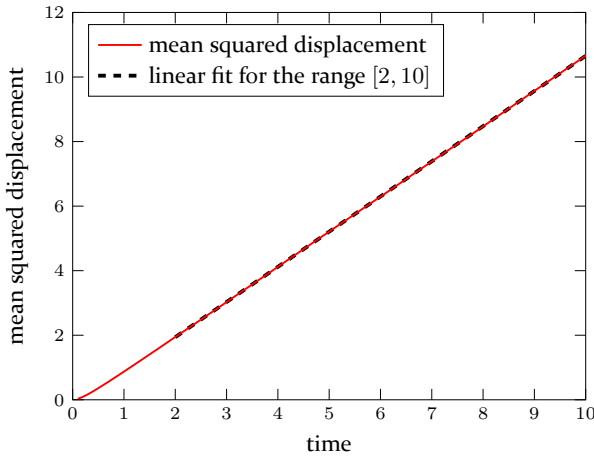
Thus, the number of coarse-graining spheres, j, a given particle is contained in, obeys a Poisson distribution with expectation value 1. Hence, while in standard SRD in each time step each particle is located in exactly one coarse-graining volume, in iSRD this is not the case, and (*iii.*) holds true only on average.

2.5.3   iSRD for the force-free case – diffusion

For the first test of the iSRD model, we consider pure diffusion in a periodic domain, being the most simple case. For this simulation and – if not specified otherwise – also for the following simulations we use the diameter of the spherical coarse-graining volume $d = (6/\pi)^{1/3} \approx 1.24$, such that $V^S = 1$. Note that this choice is arbitrary, as d is a free parameter in the model. For our choice, the simulation domain contains on average one coarse-graining sphere per unit volume. Each coarse-graining sphere contains $M = 10$ particles on average. Figure 2.3 shows the mean squared [displacement] of the particles. After a short initial transient, the mean squared displacement increases linearly with time. The dashed line shows a linear fit to the simulation data. This indicates that diffusive mass transport is reproduced correctly in iSRD.

2.5.4   iSRD for stationary Couette and Poiseuille flow – momentum transport

To demonstrate the simulation of momentum transfer with iSRD, we simulate stationary Couette flow as well as plane Poiseuille flow. In both
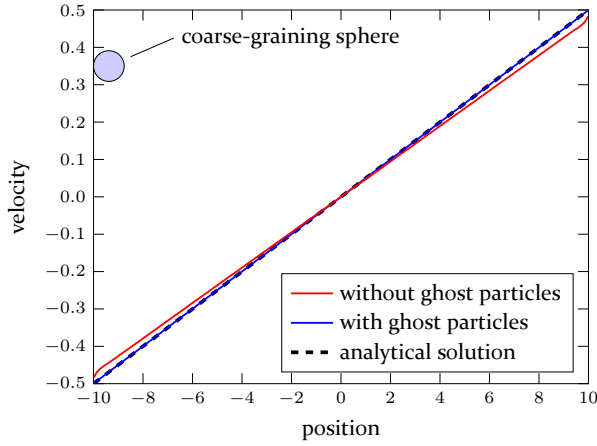
FIG. 2.3: Mean squared displacement measurement of a force-free system obtained by iSRD. The dashed line shows a linear fit to the simulation data, disregarding the initial transient. The auxiliary grid consists of $32 \times 32 \times 32$ cubic cells with side length 1.

cases, the walls are modeled through bounce-back boundary conditions [39]. Temperature is kept constant by means of the cell-level thermostat described in Refs. [40, 41]. Figures 2.4 and 2.5 show the velocity profiles obtained from the simulation together with analytical solutions for reference. The viscosity is not known a priori, and is, therefore, determined from the curvature of the flow profiles in Fig. 2.5. The channel walls are modeled both with and without ghost particles. Further details regarding this aspect are discussed in Sec. 2.5.5.
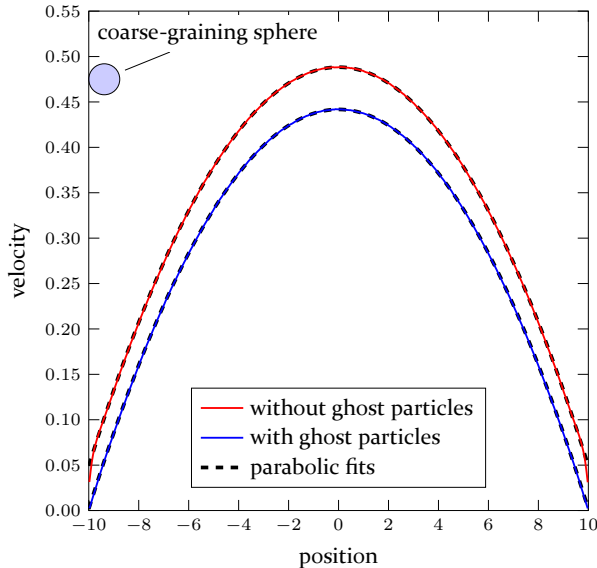
For both cases, the analytical solution given by the Navier-Stokes equations is recovered, that is, iSRD reproduces the momentum transport correctly, except for the region close to the walls, where we obtain a finite slip, unless ghost particles are employed. The flow profiles obtained from iSRD simulations are smooth and – in contrast to the upper solid line shown in Fig. 2.1 – independent [of] the underlying spatial discretization. The reason is that the iSRD scheme inherently maintains Galilean invariance.

2.5.5   Reducing slip at the walls – ghost particles

The finite slip at the system walls modeled by bounce-back boundaries is a well known problem of virtually all particle-based, computational fluid dynamics methods, see, for example, Ref. [51]. This on meso- and macroscopic scales undesirable behavior can be corrected by introducing ghost

FIG. 2.4: Couette flow simulated using iSRD with and without ghost particles. The dashed line shows the analytical solution for the given boundary velocities. The size of a coarse-graining sphere is shown at the top left.

FIG. 2.5: Plane Poiseuille flow simulated using iSRD with and without ghost particles. The dashed lines are parabolas fitted in the interval $[-5, 5]$. For the viscosity we obtain $\nu = 0.568$ with ghost particles and $\nu = 0.569$ without. In this example the Reynolds number is approximately 15.5. In dimensional quantities, this would, for example, correspond to water at room temperature ($20\,°$C) flowing through a $2\,$mm wide channel at velocity $7.8\,$mm/s.

particles [39, 52]. Here, we apply the model developed in Refs. [53, 54] for smoothed-particle hydrodynamics (SPH) simulations: In case a coarse-graining sphere reaches out of the domain and into the wall, we mirror the particles from inside the domain at the intersected boundary. The velocity of a ghost particle is computed by inverting the corresponding particle's velocity $\vec{v}_i$ with respect to the wall velocity $\vec{u}_{\text{wall}}$, that is, $\vec{v}_i^{\,\text{ghost}} = 2\,\vec{u}_{\text{wall}} - \vec{v}_i$. In order to make the interaction between fluid and wall symmetric, additional coarse-graining spheres are generated with centers located beyond the domain boundary. This effectively leads to an extrapolation of the flow velocity beyond the domain boundary.
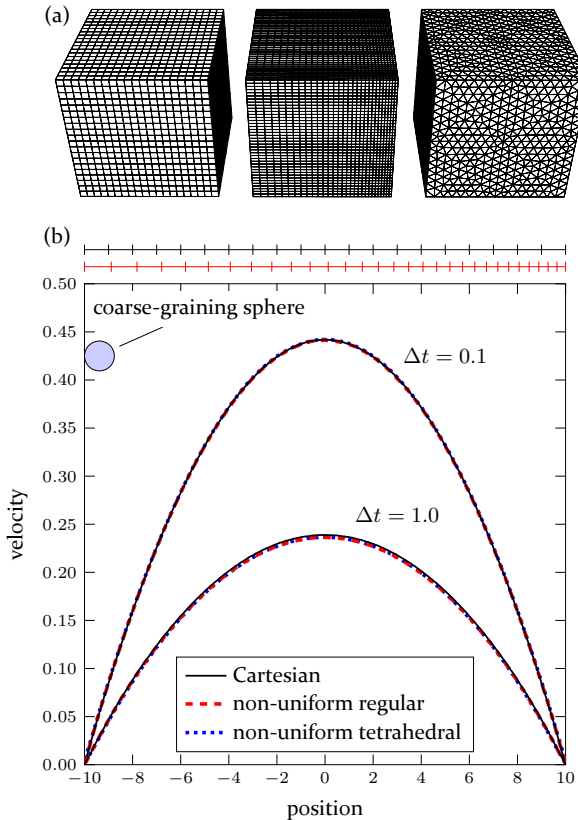
The blue lines in Figs. 2.4 and 2.5 show the flow profiles obtained by iSRD for Couette flow and plane Poiseuille flow where ghost particles are employed. In both cases, we obtain excellent agreement between the simulation results and the theoretical solution.

2.5.6 Independence of iSRD [of] the auxiliary grid

The results of iSRD do not noticeably depend on the chosen auxiliary grid. For demonstration, we compute the velocity profiles for Poiseuille flow in a cubic domain with identical parameters, except for the spatial discretization of the auxiliary grid, see Fig. 2.6 a. Three cases are investigated: A Cartesian grid (see solid black lines in Fig. 2.6 b), a non-uniform regular grid (dashed red lines), and a non-uniform tetrahedral discretization (blue dotted lines). For both considered time step sizes, $\Delta t = 0.1$ and $\Delta t = 1$, and for all grids, the velocity profiles coincide perfectly. Hence, the grid geometry does not affect the simulation results. This is not surprising, since for the case of iSRD the grid is only a data structure intended to accelerate the simulation. This makes iSRD particularly suitable for flows in domains of complex geometric shape, which cannot be meshed uniformly.

2.6 Transport Coefficients in iSRD

For standard SRD, Kikuchi et al. [48] derive an analytical expression for the kinetic contribution to the viscosity, $\nu_{\text{SRD}}^{\text{kin}}$, by considering the change of velocity correlations $\langle v_x\, v_y \rangle$ in stationary Couette flow due to the action of the streaming and the collision operators. The effect of the streaming operator is the same for SRD and iSRD, while the collision operator acts differently: In SRD at any time, each particle is located in exactly one coarse-graining volume. This is not the case for iSRD. To derive an expression equivalent to Eq. (2.7) for the case of iSRD, we consider the effect of the

FIG. 2.6: Plane Poiseuille flow simulated using iSRD, including ghost particles, for the three different auxiliary grids depicted in (a). The mesh on the left consists of cubic cells with constant width, as indicated by the black scale in (b). The red scale refers to the mesh in the center, comprising non-uniform hexahedra with square basis and varying extent in the direction of the velocity gradient, i.e., normal to the walls. The mesh on the right is composed of non-uniform tetrahedral cells.

collision operator on the velocity correlation $\langle v_x v_y \rangle_i$, referring to particle i under the condition that the particle is contained in $j \in \{0, 1, 2, \dots\}$ coarse-graining spheres. The expectation value of the kinetic contribution to the viscosity, ν_{iSRD}^{kin}, is then obtained as a weighted average of these contributions for all j.

If at a certain time step, particle i is not located in any coarse-graining sphere, that is, $j = 0$, the collision step does not change its contribution to the velocity correlation, $\langle v_x v_y \rangle_i$. If the particle is contained in exactly one coarse-graining sphere ($j = 1$) the velocity correlation changes according

to Eq. (2.7). For $j = 2$, when the particle is located in two coarse-graining spheres, S_1 and S_2, its contribution to the velocity correlation is

$$\langle v_x(t+\Delta t)v_y(t+\Delta t)\rangle_i = f(\alpha, n_{S_1})f(\alpha, n_{S_2})\langle v_x(t)v_y(t)\rangle_i \, , \qquad (2.18)$$

where n_{S_1} and n_{S_2} are the total numbers of particles in these spheres. For the general case, that particle i is contained in exactly j coarse-graining spheres, we have

$$\langle v_x(t + \Delta t)v_y(t + \Delta t)\rangle_i = \langle v_x(t)v_y(t)\rangle_i \prod_{k=1}^{j} f\left(\alpha, n_{S_k}\right)$$
$$\approx \langle v_x(t)v_y(t)\rangle_i \left[f\left(\alpha, M\right)\right]^j \, , \qquad (2.19)$$

where we employ Eq. (2.6) with the approximation that the numbers of particles contained in the coarse-graining volumes are independent. Using the probability, A_j, given in Eq. (2.17), for finding particle i in j coarse-graining spheres, and averaging over all particles, we define

$$\tilde{f}(\alpha, M) \equiv \sum_j A_j \, f^j(\alpha, M) \stackrel{Eq. \, (2.17)}{\approx} e^{f(\alpha, M)-1} \, , \qquad (2.20)$$

and find an expression for the change of the velocity correlation function due to a collision step in iSRD,

$$\langle v_x(t + \Delta t) \, v_y(t + \Delta t)\rangle = \tilde{f}(\alpha, M) \, \langle v_x(t) \, v_y(t)\rangle \, , \qquad (2.21)$$

having the same functional form as Eq. (2.7). Eventually, we obtain the kinetic contribution to the viscosity in iSRD,

$$\nu_{\text{iSRD}}^{\text{kin}} = \frac{k_B T}{m} \Delta t \left(\frac{1}{2} + \frac{\tilde{f}}{1 - \tilde{f}}\right) \, , \qquad (2.22)$$

which has the same functional form as $\nu_{\text{SRD}}^{\text{kin}}$, given in Eq. (2.3). The diffusion coefficient can be derived analogously to the kinetic part of the viscosity. We find
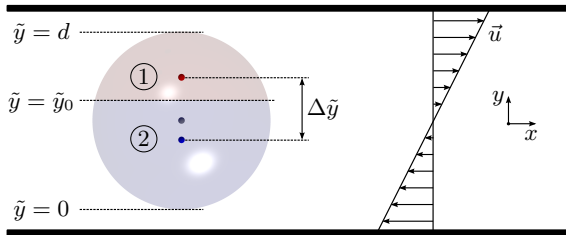
$$D_{\text{iSRD}} = \frac{k_B T}{m} \Delta t \left(\frac{1}{2} + \frac{\tilde{g}}{1 - \tilde{g}}\right) \, , \qquad (2.23)$$

with

$$\tilde{g}(\alpha, M) = \sum_j A_j \, g^j(\alpha, M) \stackrel{Eq. \, (2.17)}{\approx} e^{g(\alpha, M)-1} \, . \qquad (2.24)$$

Note that the shape of the collision bins does not affect the kinetic part of viscosity or the diffusion coefficient. The difference between iSRD and standard SRD comes merely from the fact that the number of collision bins a particle is located in per collision step is distributed differently in iSRD compared to standard SRD. Hence, knowing the size and average number of the coarse-graining volumes is sufficient to compute the kinetic part of viscosity and the diffusion coefficient.

In contrast, for the collisional contribution to viscosity, also the coarse-graining volumes' shape is important. To show this, we follow Ref. [48], and examine the redistribution of momentum due to the collision operator for stationary Couette flow with $\vec{u}(y) = [\dot{\gamma}\,y,\,0,\,0]$ and constant shear rate $\dot{\gamma} = \partial u_x(y)/\partial y$. We divide the coarse-graining sphere of diameter d into two

FIG. 2.7: Redistribution of momentum within one coarse-graining sphere in stationary Couette flow. The coarse-graining sphere is divided into two subvolumes by a horizontal plane at $y = \tilde{y}_0$.

subvolumes, ① and ②, separated by the plane $\tilde{y} = \tilde{y}_0$ with $0 \leq \tilde{y}_0 \leq d$, as shown in Fig. 2.7. The two subvolumes accommodate $n^{(1)}$ and $n^{(2)}$ particles with $n^{(1)} + n^{(2)} = n$, traveling at average velocities $\langle v_x \rangle^{(1)}$ and $\langle v_x \rangle^{(2)}$ in x-direction. The average velocity in the entire coarse-graining sphere is $\langle v_x \rangle^S$. Therefore,

$$\Delta v_x^S \equiv \langle v_x \rangle^{(1)} - \langle v_x \rangle^{(2)} = \frac{n^{(1)} + n^{(2)}}{n^{(2)}} \left(\langle v_x \rangle^{(1)} - \langle v_x \rangle^S \right) . \tag{2.25}$$

The average distance of pairs of particles picked from different subvolumes, denoted by $\Delta\tilde{y}$, is the distance of the geometric centers of the two subvolumes,
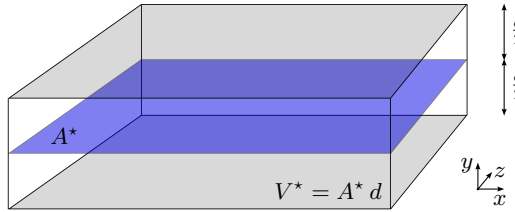
$$\Delta\tilde{y} = \frac{3\,d^3}{8\left(\frac{3}{2}\,d - \tilde{y}_0\right)\left(\tilde{y}_0 - \frac{1}{2}\,d\right)} . \tag{2.26}$$

The collision rule, Eq. (2.2), conserves momentum. Thus, the transfer of momentum between the subvolumes is equal to the change of momentum in subvolume ① due to the collision step.

The shear stress, σ_{xy}, defined as the transport of momentum per units of time and cross sectional area, is [48]

$$\sigma_{xy} = \frac{m}{A\,\Delta t} \left[\frac{2}{3} n^{(1)} \left(1 - \cos\alpha\right) \left(\langle v_x \rangle^{(1)} - \langle v_x \rangle^S \right) \right] , \qquad (2.27)$$

where m is the particle mass and A denotes the characteristic area, the momentum transfer due to one coarse-graining sphere refers to. To obtain A

FIG. 2.8: The characteristic area, A, is the average area the momentum transport within one single coarse-graining sphere refers to. The size of area A can be obtained considering the average number of coarse-graining spheres, $N^\star$, in a reference volume $V^\star \equiv A^\star d$, which is continued periodically in x and z-directions.

we consider the shaded plane, $A^\star$, in Fig. 2.8. The average number of spheres intersecting this plane is equal to the expectation value of the number of spheres, $N^\star$, having their centers located in the rectangular cuboid of volume $V^\star \equiv A^\star d$,

$$N^\star = \frac{V^\star}{V^S} = \frac{6A^\star}{\pi d^2} , \qquad (2.28)$$

thus,

$$A = \frac{A^\star}{N^\star} = \frac{\pi}{6\,d^2} . \qquad (2.29)$$

Combining Eqs. (2.25) to (2.27) and (2.29), and the average mass density in the coarse-graining sphere,

$$\rho = \frac{n\,m}{V^S} = \frac{(n^{(1)} + n^{(2)})\,m}{V^S} , \qquad (2.30)$$

we obtain the collisional contribution to viscosity,

$$\nu_{\text{iSRD}}^{\text{coll}} = \frac{\sigma_{xy}}{\rho\,\dot\gamma} = \frac{\sigma_{xy}\,\Delta\tilde{y}}{\rho\,\Delta v_x^S} = \frac{n^{(1)}\left(n - n^{(1)}\right)}{4\,n^2\,\Delta t} \frac{d^4\left(1 - \cos\alpha\right)}{\left(\frac{3}{2}\,d - \tilde{y}_0\right)\left(\tilde{y}_0 - \frac{1}{2}\,d\right)} . \qquad (2.31)$$

The number of particles $n^{(1)}$ in subvolume ① obeys a binomial distribution, $B\left(n^{(1)}|n,\,p\right)$, with probability

$$p = \frac{V^{(1)}}{V^S} = \frac{\tilde{y}_0^2\,(3d - 2\tilde{y}_0)}{d^3}\;.\tag{2.32}$$

Using the property of the binomial distribution,

$$\sum n^{(1)}\left(n - n^{(1)}\right)\,B\left(n^{(1)}|n,\,p\right) = n\,p\,(n-1)\,(1-p)\,,\tag{2.33}$$

we rewrite Eq. (2.31), and obtain

$$\nu_{\text{iSRD}}^{\text{coll}} = \frac{(n-1)\,(1-\cos\alpha)}{4n\,\Delta t} \times \frac{2d\,\tilde{y}_0^2}{\tilde{y}_0 + \frac{1}{2}d}\left[1 - \frac{\tilde{y}_0^2\,(3d - 2\tilde{y}_0)}{d^3}\right]\;.\tag{2.34}$$

Averaging over the position of the plane with respect to the coarse-graining sphere, $\tilde{y}_0$, which is uniformly distributed in $[0,\,d]$, yields

$$\nu_{\text{iSRD}}^{\text{coll}} = \frac{(n-1)\,(1-\cos\alpha)}{4\,n\,\Delta t}\frac{2\,d^2}{15}\tag{2.35}$$

and averaging over n, which is, in good approximation, Poisson distributed, leads to the final expression for the collisional contribution to the viscosity coefficient in iSRD,
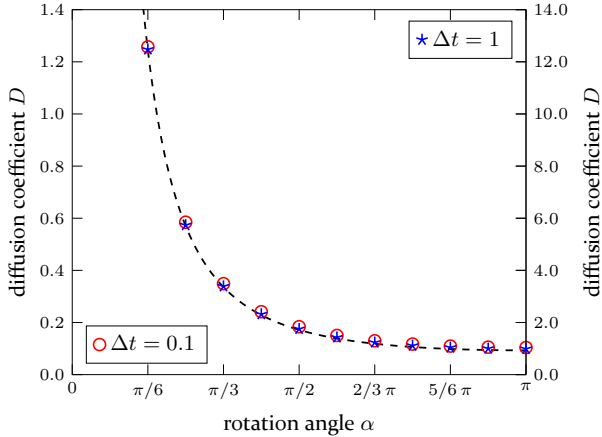
$$\nu_{\text{iSRD}}^{\text{coll}} = \frac{d^2}{30\,\Delta t}\frac{M - 1 + e^{-M}}{M}\,(1 - \cos\alpha)\;.\tag{2.36}$$

Note that Eq. (2.36) has the same functional form as the corresponding expression for standard SRD, $\nu_{\text{SRD}}^{\text{coll}}$, given by Eq. (2.10).

2.7 Quantitative Validation of iSRD

2.7.1 Benchmarking cases

To check the validity of iSRD we compare the simulation results with the derived theoretical expressions for the diffusion coefficient and the kinematic viscosity given by Eqs. (2.22), (2.23) and (2.36). We consider two physical systems, force-free fluid and plane Poiseuille flow. The parameters we vary, are the time step, Δt, the rotation angle, α, and the average number of particles per coarse-graining sphere, M. The other parameters of our simulation method, iSRD, are kept constant. We treat time and position as dimensionless parameters. Thus, the viscosity and the diffusion coefficient are considered in dimensionless form, as well.
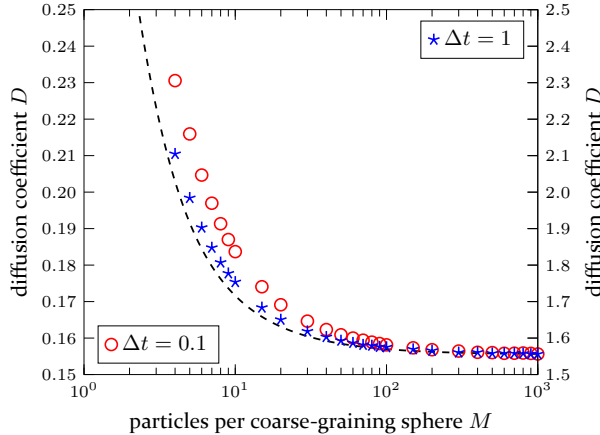
FIG. 2.9: Diffusion coefficient as a function of the rotation angle, α, for two different time steps and $M = 10$ particles per coarse-graining sphere on average. The left and right vertical axes refer to the data for $\Delta t = 0.1$ and $\Delta t = 1$, respectively. The dashed line shows the theoretical result, Eq. (2.23).

2.7.2 Diffusion coefficient

The diffusion coefficient is computed from the mean squared displacement of the particles in a cubic domain with side length 16. The simulation domain is periodically continued in all directions, and no external force acts on the particles. The numerical result is averaged over several individual measurements for each parameter set to reduce statistical errors. Two different time steps, $\Delta t = 0.1$ and $\Delta t = 1$, are considered. Fig. 2.9 shows the diffusion coefficient in dependence on the rotation angle, α. The theoretical result, given by Eq. (2.23), is indicated by the dashed line. The simulation data are in excellent agreement with the theoretical results over the full range of the rotation angle, α.
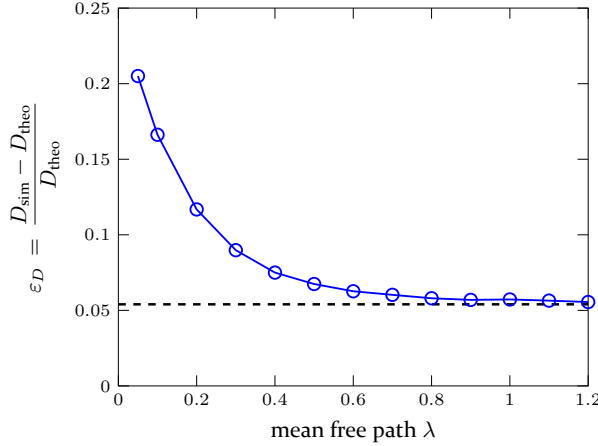
The numerical simulation results for the diffusion coefficient as a function of the average number of particles per coarse-graining sphere are shown in Fig. 2.10. For large number of particles, M, the theoretical result, Eq. (2.23), is well reproduced for both considered time steps, $\Delta t = 0.1$ and $\Delta t = 1$, indicated by the good agreement of the numerical data (symbols in Fig. 2.10) with the dashed line showing the diffusion coefficient, as given by Eq. (2.23). For smaller M, however, the simulation data deviate from the analytical results. One source for this deviation is the assumption that the number of particles within overlapping coarse-graining spheres is independent, which was exploited in the derivation of the transport coefficients. For large M,

FIG. 2.10: Diffusion coefficient as a function of the average number of particles per coarse-graining sphere, M, for two different time steps and $\alpha = \pi/2$. The left and right vertical axes refer to the data for $\Delta t = 0.1$ and $\Delta t = 1$, respectively. The dashed line shows the theoretical result, Eq. (2.23).

the relative fluctuations in particle number are small, rendering this effect negligible. At least for the smaller time step, $\Delta t = 0.1$, another influence is relevant. It is known for standard SRD, that at low particle density and small mean free path there are significant correlation contributions to the kinetic part of viscosity and diffusion coefficient. For the viscosity, this effect is masked by the collisional contribution, which is dominant in this regime. For the diffusion coefficient, which has no collisional contribution, the impact is significant [55, 44], which agrees with the results shown in Fig. 2.10.

For comparison with [55], the relative deviation between measured and predicted diffusion coefficient, ε_D, is depicted in Fig. 2.11 depending on the mean free path for $M = 5$ and $\alpha = 130°$. As the mean free path, λ, is increased, for the considered parameters, ε_D does not approach zero, but approximately 5.4%, indicated by the dashed horizontal line. One may, therefore, divide ε_D into two parts. The first one vanishes with increasing λ, and is attributed to correlations similar to what is discussed in previous works [55, 44]. In contrast, the second part does not depend on the mean free path. The source for the second part is that particle numbers in overlapping spheres are correlated, and that in the iSRD scheme a given particle may interact with other particles more than once per collision step. As Fig. 2.10 indicates, both the first and the second part of ε_D approach zero as M is increased. Moreover, comparing the results depicted in Fig. 2.11 to those
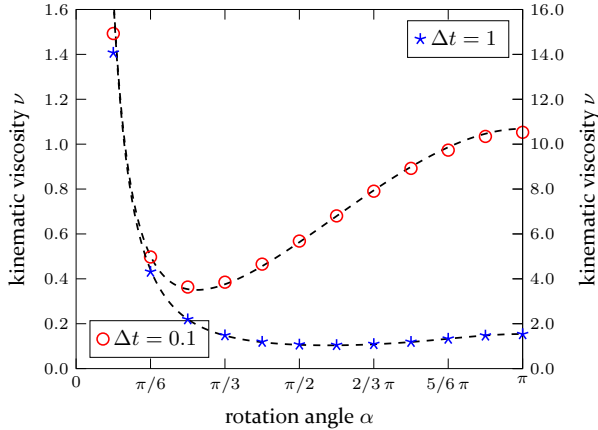
FIG. 2.11: Relative deviation between the diffusion coefficient measured in simulations, D_{sim}, and the analytical result from Eq. (2.23), denoted as D_{theo}, over the mean free path, λ, which is equal to the time step for the chosen parameters. To yield a pronounced correlation contribution, α and M are chosen as $130°$ and 5, respectively [55].
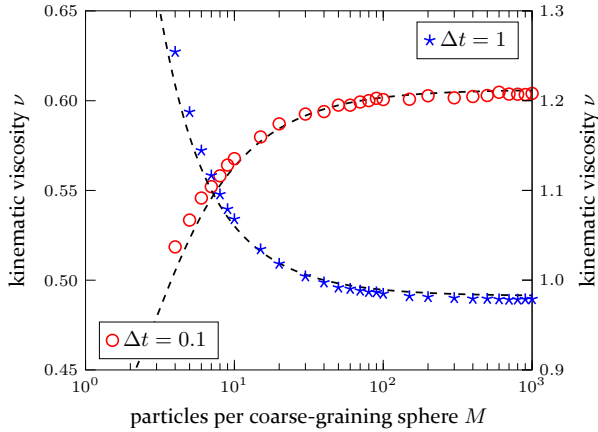
of Ref. [55] shows that for small λ, randomly distributed spheres reduce correlations more effectively than the grid-shift. In Ref. [55], the exponential term from Eq. (2.9) is neglected when computing the theoretical prediction for the diffusion coefficient, while in this study it is considered. Neglecting this term here does not change Fig. 2.11 noticeably.

2.7.3 Kinematic viscosity

We determine the kinematic viscosity from the velocity profile's curvature for plane Poiseuille flow in the steady state. The simulation domain is cubic with side length 20. The number of simulated time steps, N_t, is chosen such that $N_t M = 16 \times 10^6$, resulting in smooth profiles and small fluctuations of the viscosity. The mean free path and, thus, the transport coefficients depend sensitively on temperature. Therefore, we maintain a constant temperature by means of the cell-level thermostat described in Refs. [40, 41]. Figure 2.12 shows the simulation results for both $\Delta t = 0.1$, where the collisional contribution to viscosity dominates, and $\Delta t = 1$, where the kinetic contribution dominates. The simulation data for the viscosity as a function of the rotation angle show excellent agreement with the analytical results, Eqs. (2.22) and (2.36). For the small time step, $\Delta t = 0.1$, we obtain minor deviations, which are even less distinct for $\Delta t = 1$. Figure 2.13 shows the simulation data for the viscosity as a function of the average number

FIG. 2.12: Kinematic viscosity as a function of the rotation angle, α, for two different time steps and $M = 10$ particles per coarse-graining sphere on average. The left and right vertical axes refer to the data for $\Delta t = 0.1$ and $\Delta t = 1$, respectively. The dashed line shows the theoretical result, Eqs. (2.22) and (2.36).

FIG. 2.13: Kinematic viscosity as a function of the average number of particles per coarse-graining sphere, M, for two different time steps and $\alpha = \pi/2$. The left and right vertical axes refer to the data for $\Delta t = 0.1$ and $\Delta t = 1$, respectively. The line shows the theoretical result, Eqs. (2.22) and (2.36).

of particles per coarse-graining volume, M. We obtain minor, systematic deviations for both values of Δt, which we attribute to the thermostat, since such deviations are not apparent in the diffusion coefficient, where no thermostat is used. For the considered time steps, $\Delta t = 0.1$ and $\Delta t = 1$, the simulation results for large M deviate from the theoretical results (Eqs. (2.22)

and (2.36)) by approximately 0.3% and 0.5%, respectively. Similar to the diffusion coefficient discussed above, we also perceive systematic deviations between the simulation data and the theoretical results at small particle number. For the viscosity, this error is less pronounced than in case of the diffusion coefficient, which again matches previous findings [55, 44].

2.8 Performance study

To give an idea about the computational performance of iSRD, we compare it to traditional SRD, simulating fluid at rest within a cubic domain with side length 20 and periodic boundaries in all directions. Both implementations are based on an existing simulation framework [13].

In our SRD implementation each time step comprises the following sub steps: First, the particles are propagated according to their current velocity (*streaming step*). In this step also the periodic boundary is imposed. Second, the particles are sorted into the shifted grid in order to compute the cell-averaged velocities, which are needed to perform the multi-particle collision. Third, the relative particle velocities are rotated (*collision step*). Finally, a cell-level thermostat [40, 41] is applied to the non-shifted grid keeping the average temperature constant. The cell width is $a = 1$, and the simulation grid is aligned with the cubic domain.

The procedure for the iSRD simulations is very similar. However, the second and third step are replaced by the algorithm described in Secs. 2.5.1 and 2.5.2. As auxiliary grid and also for the thermostat, the non-shifted grid from the SRD simulations is used. For a fair comparison, the volume and number of collision bins should be equal. The coarse-graining sphere diameter is, therefore, chosen as $d = (6/\pi)^{1/3} \approx 1.24$, resulting in $V^S = 1$.

On average $M = 10$ particles are in each collision volume. We choose the time step and the rotation angle as $\Delta t = 0.1$ and $\alpha = \pi/2$, respectively. Each simulation runs for 10^4 time steps on an Intel® Core™ i7-4790K processor. Restricting to one single thread, we find iSRD to be approximately twice as time consuming as standard SRD. Increasing the number of threads, SRD and iSRD scale similarly.

2.9 Conclusion

We have introduced isotropic SRD, which is a modification of standard SRD. Instead of using Cartesian grid cells as coarse-graining volumes, we generate coarse-graining spheres randomly within the simulation domain.

This allows to maintain Galilean invariance without the need for a grid-shift. The proposed particle-based fluid simulation method is isotropic by construction and truly grid-free. Merely an auxiliary grid is needed in order to efficiently sort the particles into the coarse-graining spheres. While the structure of the auxiliary grid can affect the computational cost, we demonstrate that it does not affect the simulation results. The proposed algorithm is, therefore, particularly suitable to simulate the fluid flow through domains of complicated shape.

Moreover, we show that iSRD reproduces both mass and momentum transport correctly. We also provide analytical expressions for the transport coefficients depending on the simulation parameters. The measured values for the transport coefficients accurately follow these expressions, especially for higher particle numbers per coarse-graining volume. Further, the use of spheres as coarse-graining volumes prevents the existence of preferred directions for momentum transport, yielding a fully isotropic simulation method, even for situations with large gradients.

For both iSRD and SRD, the mean free path does not depend on the density, and therefore, the known dependence of the transport coefficients in gases on density and temperature is not recovered. Introducing an additional temperature-dependent collision probability, as proposed by Gompper et al. [25], allows to control the time step Δt locally. Since the diffusion coefficient is proportional to Δt, this idea renders the diffusion coefficient freely adjustable. Viscosity, however, cannot be adjusted similarly, because it has one component proportional to Δt and another one proportional to $1/\Delta t$. In iSRD the diameter of the coarse-graining spheres is, in principle, locally adjustable, as well. Exploiting this should allow to recover the right dependence for the viscosity. The concrete implementation is, however, not straight forward, since changing the diameter also changes the average particle number per coarse-graining volume. For the relations introduced in Sec. 2.6 to hold, the number density of coarse-graining spheres has to be adjusted accordingly, so that each particle is on average contained in one coarse-graining volume per collision step. In addition to time step and diameter, one can also adjust the rotation angle locally, yielding three control parameters in total. Following this approach, iSRD is expected to be able to simultaneously reproduce not only the correct density and temperature dependence for the diffusion coefficient and the viscosity, but also for the heat conductivity." [24]

3 Inlet and outlet boundary condition

In this chapter, we introduce a novel method for the numerically stable modeling of open boundaries for mesoscopic particle-based flow simulations, including volume conserving chemical reactions. To this end, we connect inlet and outlet via a modified periodic boundary condition allowing for discontinuities in the concentration field, while density, velocity, and temperature are strictly periodic. This novel type of boundary condition generates a concentration field corresponding to the situation that the domain is continued periodically in the main flow direction.

3.1 Introduction

In particle-based fluid simulation methods, open boundaries can be challenging, since – unless considering the outflow into vacuum – particles are not only leaving, but also entering the domain. Ignoring this effect leads to serious errors especially at flow velocities below the speed of sound. The most basic case are Dirichlet boundary conditions, i.e., density, velocity, and temperature at the boundary are given. In this case, the particles which are injected into the domain can be drawn from a biased probability distribution function [56]. For many engineering applications, however, not all macroscopic fields at the boundary are known a priori, and Dirichlet boundary conditions are not applicable. In this case, it is no longer trivial to model numerically stable, open boundaries [57]. For example, pressure boundary conditions, for which the velocity field is not prescribed, tend to induce instabilities, especially for small Mach numbers [58, 19].
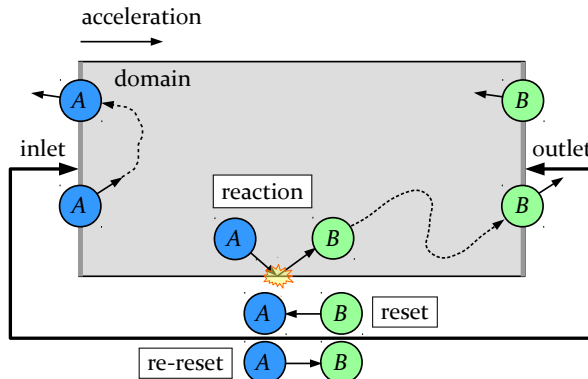
If the considered domain is periodic in flow direction, and the Mach number is small, i.e., the fluid is incompressible, one can apply periodic instead of open boundaries, and an acceleration instead of an actual pressure gradient. This procedure, however, enforces the periodicity on all fields. While this typically is acceptable for density, velocity, and temperature, it is highly undesirable for the concentration field in reactive flow, for example, through a catalytic converter with globally periodic structure.

Therefore, we develop a boundary condition, which is periodic regarding density, velocity, temperature, and pressure, while allowing the concentration field to have a discontinuity at the interface connecting inlet and outlet of the periodic simulation domain.

We will, first, discuss the algorithm underlying this novel boundary condition. Consequently, the developed boundary condition will be validated for gas flow including chemical surface reactions.

3.2   Algorithm

We develop a boundary condition which allows for discontinuities regarding the concentration field, while acting as a periodic boundary on the remaining quantities, namely: velocity, temperature, density and pressure. The

FIG. 3.1: Modus operandi of the boundary condition with species reset for the chemical reaction $A \to B$. An acceleration can be used to simulate a pressure gradient driving the flow. In this sketch the reactions happen at a surface, as in heterogeneous catalysis. However, the boundary condition works equally for reactions in the bulk.

modus operandi of this partially periodic boundary does not depend on the particular simulation method used. It works equally for all mesoscopic, particle-based simulation methods. The proposed boundary condition acts on pairs of the form *reactant species/product species*. For this concept to work, the chemical reaction has to be volume preserving, i.e., the number of product particles must equal the number of reactant particles. Consider, for example, the chemical reaction: $A_1 + A_2 + ... + A_n \to B_1 + B_2 + ... + B_n$. The periodic boundary condition with species reset would in this case act on the pairs A_1/B_1, ..., A_n/B_n, separately.

For illustration, we consider the most simple volume preserving chemical reaction: $A \rightarrow B$. In case a particle of type A undergoes a chemical reaction, it changes its species to B. Fig. 3.1 illustrates the modus operandi, assuming that the reactions take place at the top and bottom boundary. However, the boundary condition is also applicable for reactions taking place in the bulk. For the following description of the algorithm, `species` is the current particle species, that is, A or B. The `product_species` is the species assigned after reaction. Thus, the `product_species` is always B, in this example. The `target_species` is the species that has to be assigned to the particle after *reset*, following on a reaction, or after *re-reset*, in turn following on a reset. These two conversions, *reset* and *re-reset*, are described in more detail below. The variable `passes` counts how often a particle has passed through the simulation domain since the last reaction. Passes in main flow direction count positively, while passes against flow direction count negatively.

The following three events have to be conducted:

i. particle undergoing a ┃reaction┃

    if (passes $\neq 0$) **then**
    ┃   target_species := species;
    end
    species := product_species;
    passes := 0;

In case a particle undergoes a chemical reaction, the `target_species` is set equal to `species`, only if this is the first reaction since the last reset (passes $\neq 0$). This ensures that for serial reactions $A \rightarrow B$ and $B \rightarrow C$ the `target_species` is not changed to B, but remains A, even after the second reaction, $B \rightarrow C$, has taken place. During the reaction, the species of the particle is set to `product_species`, and, consequently, `passes` is set to zero.

ii. particle hitting the outlet $\Rightarrow$ ┃reset┃

    if (passes $= 0$) **then**
    ┃   swap (target_species, species);
    end
    ++passes;

In case a particle impinges on the outlet, directly after undergoing a chemical reaction (passes $= 0$), `target_species` and `species` are

exchanged. For every particle hitting the outlet, `passes` is uncondi-
tionally incremented.

iii. particle hitting the inlet $\Rightarrow$ re-reset

 if (passes = 1) **then**
  | swap (`target_species`, `species`);
 end
 if (passes > 0) **then**
  | $--$`passes`;
 end

In case a particle impinges on the inlet, directly after undergoing a
reset (`passes` = 1), `target_species` and `species` are exchanged. For
every particle hitting the outlet, `passes` is decremented, as long as it
is not falling below zero.

Decrementing and incrementing the variable `passes` at inlet and outlet is
not performed symmetrically. In case `passes` is less or equal to zero, is
not be decremented, yielding that `passes` is non-negative for all times. The
consequence of this strategy is that:

 ▷ A particle, having passed N times through the domain along the main
  flow direction, has to go in the other direction $N - 1$ times before it
  gets a re-reset.

 ▷ A particle, having passed N times through the domain against the
  main flow direction, has to go in the other direction only once to get a
  reset.

To understand the reasoning behind this discrimination, we follow the
events occurring along the trajectory of an individual particle of species A.
After some time, the particle reacts, changes its type to B, and `passes` is
set to zero. Note that the considered mesoscopic particle-based simulation
methods explicitly model the diffusive particle transport. Thus, if inlet and
outlet were connected by a normal periodic boundary condition without
reset mechanism, `passes` would follow a one-dimensional random walk
without any barrier from above or below[1]. Eventually, `passes` would diverge
either in positive or negative direction. Keeping this in mind, consider the

---

[1] Note that in case an external acceleration is applied, the random walk is biased by the flow
field.

proposed boundary condition for inlet and outlet. As defined above, reset and re-reset are conducted at `passes = 0` and `passes = 1`, respectively. Hence, to make sure the particles keep interacting with the presented boundary condition, an upper and lower barrier are required to prevent `passes` from diverging. An upper barrier for `passes` is already contained in the reset mechanism. Each particle moving in positive direction after reaction experiences a reset as soon as it hits the outlet. In this case, the particle species is set to *A*, and eventually another reactions occurs setting `passes` to zero. An analogous mechanism is missing for particles moving in negative direction. In this case, the particle species would remain *B*, and `passes` would be able approach negative infinity. To avoid this, we introduce an explicit lower bound for `passes`. Without this explicit lower bound, `passes` has been observed to approach negative infinity for all reacting particles in the domain. This observation has been made both with and without using an external acceleration to drive the flow.

In real chemical reactions, $A_1 + A_2 + ... + A_n \rightarrow B_1 + B_2 + ... + B_n$, the particle properties change typically. In principle, the proposed model allows for the particle mass to change during the reaction, that is, $m_{A_i} \neq m_{B_i}$. In this case, to keep the temperature continuous, the thermal velocity of the particles has to be adjusted not only after the reaction but also after reset and re-reset. This requires an extra thermostat at the inlet and outlet.

3.3 Validation

3.3.1 First order reaction
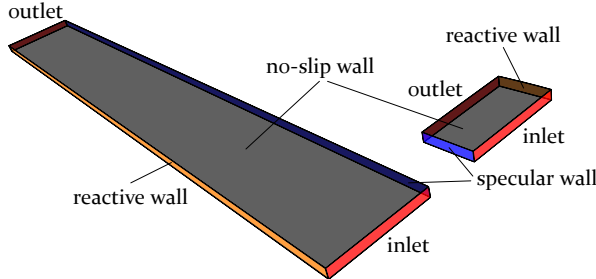
In the following test scenario, we simulate heterogeneous catalysis, and the reactions are bound to the *reactive walls* shown in Fig. 3.2. In the mass transfer limited regime, this allows us to observe distinct concentration profiles, which we will use to validate the algorithm. We will compare the mole fraction profiles in two different channels which are identical, except for their length. The mole fraction corresponding to the ith species is defined as

$$x_i = \frac{n_i}{\sum_j n_j} \, , \tag{3.1}$$

where n_i is the number density of the ith species and $\sum_j n_j$ is the total number density.

The two channels, together with the applied boundary conditions, are depicted in Fig. 3.2. The longer channel, denoted as *reference*, consists of $40 \times 4 \times 320$ cubic cells, while the shorter one, denoted as *segment*, comprises
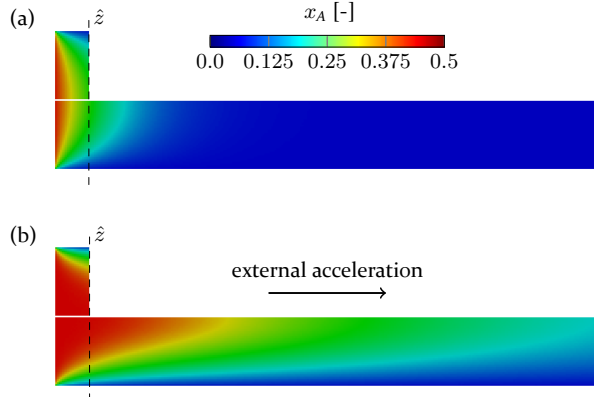
FIG. 3.2: The length of the reference channel equals sixteen times the length of the segment. Inlet and outlet are connected via the proposed periodic boundary condition with species reset.

only $40 \times 4 \times 20$ cubic cells. The cell width, $a = 1$, is equal for both channels. The gas dynamics is simulated using Direct Simulation Monte Carlo (DSMC) [16] with mean free path, $\lambda = 1$, equal to the cell width.
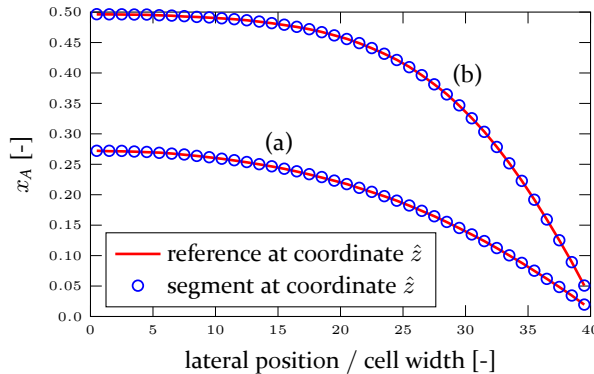
The surface reaction, we consider, is $A \rightarrow B$, as shown in Fig. 3.1. In case a particle of type A impinges on the reactive surface, it changes its type to B and immediately leaves the surface again. We initialize both domains with 10 particles of type A and 10 particles of type B per simulation cell. This choice adjusts the reactant mole fraction, x_A, at the inlet homogeneously to 50 %. For both cases, inlet and outlet are connected via the periodic boundary condition with species reset, described above.

To evaluate the influence of flow velocity, we consider two different cases: First, we set the external force to zero, i.e., we consider pure diffusion. Second, the flow is driven by an external acceleration, substituting a pressure gradient. Denoting the speed of sound as c_s, superficial and maximum velocity in the channel are $0.14\,c_s$ and $0.19\,c_s$, respectively. The resulting mole fraction fields are shown in Fig. 3.3 (a) and (b).

In both cases – with and without external forcing – the reactant mole fraction in the segment reveals no visible difference compared to the corresponding reference channel in Fig. 3.3. Moreover, Fig. 3.4 shows that even right at the segment's outlet, coordinate $\hat{z}$, the observed mole fraction profiles coincide exactly with the curves extracted for the reference channel. Therefore, we conclude that the periodic boundary with species reset gives the correct mole fraction profile at the outlet, assuming a periodic continuation of the domain.
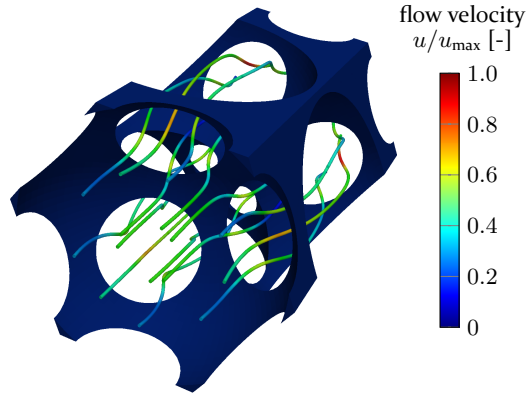
FIG. 3.3: Comparison between the reactant mole fraction, x_A, in the segment (small domain) and that in the corresponding reference channel (large domain). In (a) we have pure diffusion, while in (b) the flow is driven by an external acceleration.

FIG. 3.4: Comparing the reactant mole fraction profiles at the coordinate $\hat{z}$, which corresponds to the segment's outlet. The labels, (a) and (b), refer to the two setups from Fig. 3.3.

3.3.2 Second order reaction

To indicate the potential of our approach, we also provide a more challenging example, namely the low-temperature water-gas shift, as characterized in [21], in an open-cell porous foam structure, modeled as regular inverse sphere packing [14]. As before, we compare two different system sizes: one unit foam cell versus two unit foam cells in a row. The gas dynamics is simulated with isotropic stochastic rotation dynamics (iSRD) [24]. The gas flow, which is visualized in Fig. 3.5, is again driven by an external
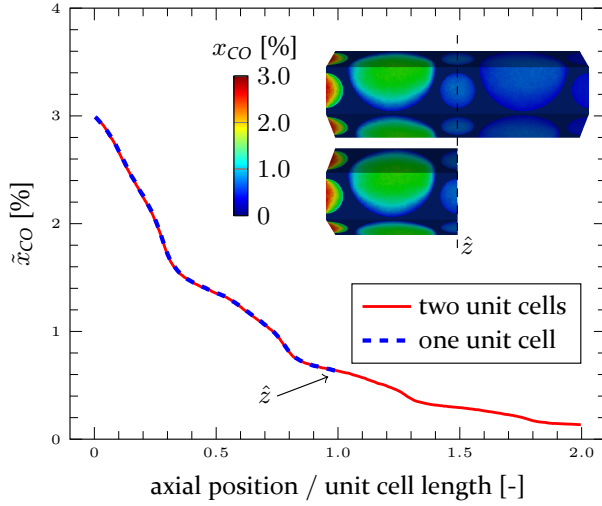
FIG. 3.5: Streamlines for gas flow in an open-cell porous foam structure modeled as inverse sphere packing using constructive solid geometry (CSG). The considered structure is described in more detail in Sec. 4.2.1.

acceleration, resulting in the superficial and maximum velocity being $0.10\,c_\mathrm{s}$ and $0.30\,c_\mathrm{s}$, respectively. The pore size Reynolds number is defined as
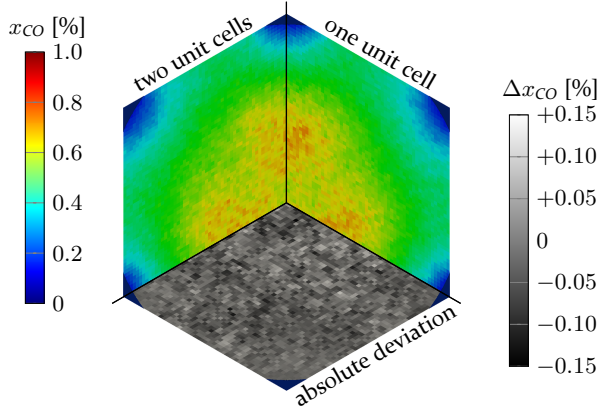
$$\mathrm{Re} = \frac{d_\mathrm{p}U}{\nu}\,, \tag{3.2}$$

where the pore size, d_p, is defined as the distance between the sphere centers, U is the superficial velocity, and ν denotes the kinematic viscosity. For the regarded setup, $\mathrm{Re} = 26$, while the Schmidt number is 0.77. The considered reaction is $CO + H_2O \rightarrow CO_2 + H_2$. The local reaction rate is high enough to push the system into the mass transfer limited regime, i.e., practically all encounters of CO and H_2O at the surface lead to a reaction. The inflow mole fractions of the reactants are $x_{CO} = 3\,\%$ and $x_{H_2O} = 26\,\%$.

In this case, where the reactants' inlet concentrations differ, re-reseting must be synchronized, such that the average number of re-resets is equal for all reactants. For second order reactions with differing reactant concentrations at the inlet, this can be achieved by the following procedure. In each boundary cell we count the number of re-resets per species, and we allow a re-reset for the abundant species, H_2O, only if the rarer species, CO, has had a greater or equal number of re-resets already. Following this rule, we will allow re-resets for the rarer species in advance due to thermal fluctuations. However, this does not corrupt the synchronization, since the abundant species will always catch up subsequently.

FIG. 3.6: Particle flow rate attributed to *CO* over total particle flow rate in an open-cell porous foam structure. The inset shows the mole fraction of *CO* in the two considered systems.

FIG. 3.7: This figure refers to the cross section at coordinate $\hat{z}$. Due to symmetry, it is not necessary to consider the unit cell's complete cross section. For the two different setups, the two upper segments show the mole fraction profiles at the coordinate $\hat{z}$, which corresponds to the outlet in case of simulating one unit cell. The lower segment shows the deviation between both profiles.

To assess this approach, in Fig. 3.6, we examine the consumption of *CO* along the main flow direction. Instead of the mole fractions, we consider the ratio between the particle flow rates,

$$C_i(z) = \frac{\int_{S(z)} n_i \, u \, ds}{\int_{S(z)} \sum_j n_j \, u \, ds} , \tag{3.3}$$

depending on the position along the main flow direction, z. The integral runs over slices, $S(z)$, which are perpendicular to the main flow direction. The velocity component in main flow direction is denoted as u, while ds is the surface element normal to the main flow direction. Again the two compared simulation setups only differ in domain length. Any artifacts due to the presented boundary condition should be visible at the outlet of the shorter domain, position I. Additionally, in Fig. 3.7 we regard x_{CO} directly at the coordinate $\hat{z}$ marked in Fig. 3.6. The deviations, $\Delta x_{CO} = x_{CO}^{\text{one cell}} - x_{CO}^{\text{two cells}}$, show random fluctuations around zero mean.

3.4 Conclusion

In this chapter, we have introduced a numerical method to simulate open boundaries in reactive flow through geometrically periodic domains. To this end, we connect inlet and outlet via a partially periodic boundary, allowing for discontinuities in the concentration fields. The concentration field emerging due to the proposed boundary condition corresponds to a channel, which is periodically continued at the outlet, and has a homogeneously mixed inflow. Our boundary condition is not as general as the characteristic boundary condition suggested in [57]. However, it is unconditionally, numerically stable, and, as opposed to the approach in [57], no partial differential equations have to be solved for inlet and outlet. For some applications, homogeneous velocity and concentration fields may be desired not only at the inlet but also at the outlet, mimicking a reservoir with an unknown, spatially constant concentration value at the outlet. This can be achieved by inserting each particle at a random position, after transition through the modified periodic boundary condition.

This boundary condition will serve as inlet and outlet for the unit foam cell simulations performed in the next two chapters.

4 Low temperature water-gas shift reaction

In this chapter, we investigate heterogeneous catalysis in open-cell foam structures, modeled as inverse sphere packings. The foam geometry is described analytically using Constructive Solid Geometry (CSG). The gas dynamics is simulated with isotropic Stochastic Rotation Dynamics (iSRD) presented in Chap. 2. Inlet and outlet are connected via the modified periodic boundary condition from Chap. 3 allowing for discontinuities in the concentration field, while the density, temperature and the velocity fields are strictly periodic. After validating our simulation model based on experimental results from the literature, we investigate the low temperature water-gas shift reaction following the Langmuir-Hinshelwood reaction mechanism. Considering typical reaction parameters from literature, we find for the considered Reynolds number that the catalyst density in the washcoat may be reduced by the factor 100 without notable loss of conversion efficiency. Further reduction, however, pushes our prototype setup towards the reaction rate limited regime leading to a significantly declined conversion rate. For a certain pore size Reynolds number, the foam porosity is varied to determine optimum open-cell foam structures, which combine low flow resistance and high conversion efficiency. Large porosity values are found favorable in both the mass transfer limited regime and in an intermediate regime. Moreover, as the porosity is increased, the ratio between conversion and required reactive surface area increases as well. Compared to the mass transfer limited regime, in the intermediate regime, the dependence of the surface utilization on the porosity is less pronounced.

4.1 Introduction

In heterogeneous catalysis, the catalyst is applied to solid support structures. In this context, open-cell metal foams are extremely promising. As a result of their high tortuosity and specific surface, such foam structures provide excellent mass transfer properties [5]. Moreover, the high porosity keeps the associated flow resistance comparatively small [6]. The performance of

open-cell foams for heterogeneous catalysis has been investigated in various experimental studies [6, 7, 8]. Furthermore, several numerical studies have been performed with continuum simulation methods modeling the foam structure as Kelvin cells[1] [11, 5, 9, 10].

As opposed to this, we employ isotropic Stochastic Rotation Dynamics, a particle-based simulation technique, to simulate the reactive gas flow in unit foam cells [24]. The unit foam cell is modeled as an inverse sphere packing. Smorygo et al. [14] show that this approach yields good predictions for the specific surface and the hydraulic permeability of open-cell foam structures. Constructive Solid Geometry (CSG) is used to describe the complex shaped boundary independently of the spacial resolution of the simulation domain [15]. This allows us to evaluate the chemical reactions exactly at the analytically defined reactive surface. The surface described with CSG is assumed to correspond to the exterior surface of an even $CuO/ZnO/Al_2O_3$ washcoat layer applied to an underlying foam structure. As prototype reaction, we consider the low temperature water-gas shift. We implement an effective reaction model assuming the reactions to take place within the porous washcoat, which is not simulated explicitly. The reactions are assumed to follow the Langmuir-Hinshelwood reaction mechanism [20, 21]. This study is not restricted to the mass transfer limited regime, but also considers the reaction rate limited regime. Therefore, the reaction mechanism has to be modeled in detail. We compute the effective reaction rate in the washcoat layer based on precomputed look-up tables for the effectiveness factor [22]. Apart from the effectiveness factor, the effective reaction rate depends on several model parameters, on the temperature, and on the reactants' partial pressures at the exterior washcoat surface. While the model parameters and the temperature in the washcoat are prescribed explicitly, the partial pressures are computed from the collision fluxes on the surface. Hence, all relevant quantities are evaluated directly at the reactive boundary.

Note that, unless the fields on the boundary are known explicitly, it is not trivial to model open boundaries in particle-based methods [57]. This problem can be circumvented by using periodic instead of open boundaries and an acceleration instead of an actual pressure difference. However, periodic boundaries naturally imply that the concentration field is equal at inlet and outlet, which is not applicable for reactive flow simulations. Therefore, we use the novel boundary conditions from Chap. 3, which are periodic regarding velocity, temperature, density and pressure while allowing the

---

[1] A sketch of this structure is provided in [11].

concentration field to have a discontinuity at the surface connecting inlet and outlet.

In this chapter, we first concisely describe the main components of our simulation model. Second, we validate the individual parts of our model using data from the literature. Subsequently, we consider the low temperature water-gas shift reaction in porous foam for typical parameters. We vary both the active site density within the washcoat and the porosity of the considered unit foam cell. In [11] Lucci et al. find that in the mass transfer controlled regime the dimensionless performance index monotonously increases with porosity. We will assess this statement for low temperature water-gas shift, and see how far we can extend its validity towards the reaction rate limited regime.

4.2 Methods

In order to validate the simulation results in Sec. 4.3 and to evaluate the gathered results in Sec. 4.4, several dimensionless numbers have to be introduced. An overview over the dimensionless numbers used in this
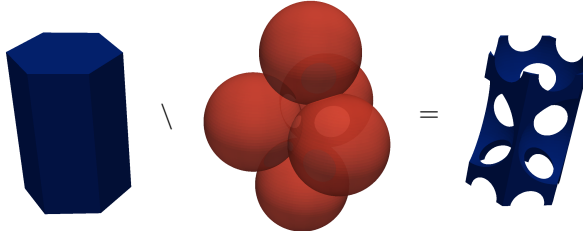
Table 4.1: Overview over the dimensionless numbers used throughout this thesis.

name	symbol	definition
Reynolds number	Re	$\dfrac{\text{convective transport rate}}{\text{diffusive momentum transport rate}}$ $= \dfrac{\text{inertial forces}}{\text{viscous forces}}$
Péclet number	Pe	$\dfrac{\text{convective transport rate}}{\text{diffusive mass transport rate}}$
Schmidt number	Sc	$\dfrac{\text{diffusive momentum transport rate}}{\text{diffusive mass transport rate}}$
Hagen number	Hg	dimensionless pressure gradient in forced flow
Euler number	Eu	$\dfrac{\text{pressure forces}}{\text{inertial forces}}$
Sherwood number	Sh	$\dfrac{\text{mass transfer rate to the reactive surface}}{\text{diffusive mass transport rate}}$
Thiele modulus	Φ	$\left(\dfrac{\text{reaction rate}}{\text{diffusive mass transport rate}}\right)^{1/2}$

thesis is provided in table 4.1. Before the obtained results are discussed, the simulation model has to be considered first. The employed model is implemented based on the framework developed in [13], which is capable of robust event-driven particle tracking in complex geometries. In order to numerically investigate heterogeneous catalysis in foam structures we need to couple gas dynamics within complex geometries and reaction kinetics at the catalytic surface. Smorygo et al. show that inverse sphere packings are an excellent model for open-cell porous foam structures [14]. Hence, the reactive boundary can be described using constructive solid geometry. In the following subsections we give a short overview over the individual ingredients of our simulation model.

4.2.1 Geometry model

As suggested by Smorygo et al. [14] we model the open-cell foam structure as an inverse sphere packing, shown in Fig. 4.1. This approach allows us to fully parametrize the geometry by the prism width d_p and the sphere diameter d. The porosity of the foam, ε, can be adjusted by changing the ratio $k = d_p/d$, while the underlying auxiliary grid remains unchanged. The prism width, d_p, plays the role of the pore size in a real foam sample. Hence, the

FIG. 4.1: The open-cell foam structure is modeled as an inverse sphere packing. The foam porosity depends only on the ratio between the sphere diameter and the width of the prism.
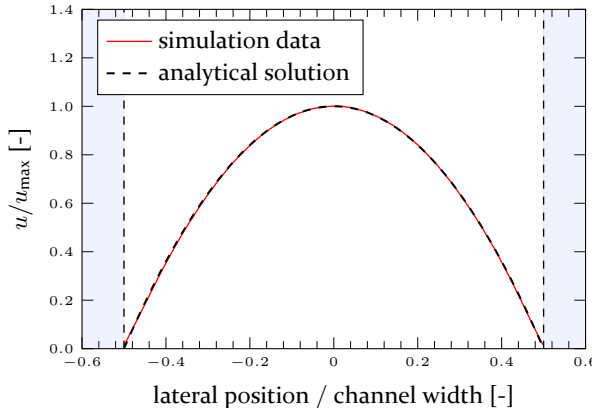
geometry is easily adjustable and decoupled from the simulation grid. This concept works especially well for particle-based simulation methods, where the boundary conditions can be enforced directly on every particle hitting the wall. Moreover, this approach allows us to evaluate the partial pressure corresponding to each individual particle species exactly at the surface via the collision fluxes, i.e., simply by bookkeeping over the particles having hit the wall.

4.2.2 Gas dynamics

Fluid model. The gas dynamics is simulated with isotropic Stochastic Rotation Dynamics (iSRD) [24], a modification of standard Stochastic Rotation Dynamics (SRD) [18, 25]. SRD has been shown to be suitable to model fluid flow through complex geometries [39, 59] . In both methods the fluid is modeled using point-like quasi-particles which do not directly correspond to actual particles, but represent a discretization of the phase space. Each time step comprises one streaming step, propagating the particles according to their current velocity, and one collision step, allowing the particles to exchange momentum. The streaming step is identical both in SRD and iSRD. However, for the collision step, in iSRD the particles are grouped into randomly distributed spheres, and not into the cubic cells of a Cartesian simulation grid as in SRD. The process of sorting the particles into the collision spheres can be enhanced significantly by an auxiliary mesh. Employing an auxiliary mesh is not compulsory, however, and it does not affect the simulation result, i.e., iSRD is grid free. More importantly, iSRD does not suffer from anisotropy at complex shaped domain boundaries [24].

Inlet and outlet. The outlet of the simulation domain is connected to the inlet via a specialized semi-periodic boundary condition, which has been designed particularly for reactive gas flow. While enforcing periodicity on density, velocity, temperature and pressure, it allows for a discontinuity in the composition of the simulated gas mixture. This boundary condition ensures temporally constant reactant and product concentrations at the inlet. Conversely, the concentration profiles at the outlet automatically resemble a periodical continuation of the domain in flow direction Chap. 3.
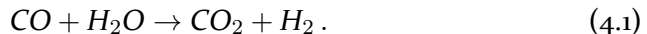
Solid wall. In order to avoid slip at the solid wall, whenever a particle hits the wall, its velocity is inverted before the particle is released again. However, in case the collision bins – in our case collision spheres – overlap with the domain boundary, this procedure is not sufficient to ensure no slip at the wall [39]. Therefore, we randomly generate ghost particles within the solid walls. The ghost particle velocities are chosen from a Maxwellian distribution with zero average velocity. The ghost particle density is equal to the bulk density [52]. In Fig. 4.2, we show the simulated flow profile for plane Poiseuille flow. The shaded area indicates the region in which ghost particles have been distributed. The simulation data shows no significant deviations from the analytical solution.

FIG. 4.2: We simulate plane Poiseuille flow, in order to validate our implementation of the no-slip boundary condition at the solid wall.

4.2.3 Reaction Model

Due to its industrial relevance we investigate the *low temperature water-gas shift reaction*, i.e., the formation of carbon dioxide and hydrogen from carbon monoxide and steam,

$$CO + H_2O \rightarrow CO_2 + H_2 \,. \tag{4.1}$$

The back reaction is not taken into account. According to Ayastuy et al., this reaction follows the *Langmuir-Hinshelwood* reaction path [21]. This is one of the most important prototype reaction path for heterogeneous catalysis. Hence, the results and conclusions attained here are applicable to other catalytic reactions as well. In industrial applications the carrier structure is typically coated with a porous washcoat layer. This washcoat provides a large internal surface containing the catalytic sites necessary for the water-gas shift reaction to take place. We assume the foam structure to be coated evenly denoting the washcoat layer thickness by L. Since the reactant concentrations decrease with increasing depth in the washcoat, the local reaction rate, $\dot{n}_{\mathrm{r}}$, in the washcoat, which is defined as the number of reactions per time and washcoat volume, varies as well. Note that, considering the Langmuir-Hinshelwood mechanism, the reaction rate is not necessarily a monotonous function of the reactant concentrations [22].

The gas flow through the mesoporous foam structure is simulated as described in Sec. 4.2.2. It is not feasible to model the open-cell foam and the washcoat simultaneously, since the associated processes occur on different

scales. Hence, the reaction diffusion process within the washcoat is not modeled live during the simulation, but we decouple it from the actual simulation by introducing an effective model for the reactions. Ignoring the back reaction, the average reaction rate in the washcoat layer is given by

$$\langle \dot{n}_{\mathrm{r}} \rangle = \zeta \, \frac{k \, P_{CO} \, P_{H_2O}}{(1 + K_{CO} \, P_{CO} + K_{H_2O} \, P_{H_2O} + K_{CO_2} \, P_{CO_2} + K_{H_2} \, P_{H_2})^2} \,, \quad (4.2)$$

where P with subscript refers to the corresponding species' partial pressures at the outer surface of the washcoat. The average reaction rate has units of $\mathrm{mol/(m^3 \, s)}$. The reaction rate constant and the adsorption constants are denoted as k and K with corresponding subscript, respectively. The fraction in Eq. (4.2) corresponds to the local reaction rate at the outer surface of the washcoat. The effectiveness factor, ζ, is the ratio between the average reaction rate within the washcoat layer, $\langle \dot{n}_{\mathrm{r}} \rangle$, and the local reaction rate at its outer surface [60].

We follow the procedure described in [22] to precompute the effectiveness factor in the relevant parameter range of the partial reactant pressures and the model parameters, which vary with temperature. Note that to compute the effectiveness factor for a given parameter set, the one-dimensional reaction-diffusion equation for Langmuir-Hinshelwood kinetics in the washcoat has to be solved, while the reaction rate directly at the surface can be evaluated very easily.

The domain boundary described by the inverse sphere packing is assumed to correspond to the outer surface of the washcoat. The reactive boundary is discretized into individual boundary cells. To eliminate fluctuations, the partial surface pressures are computed from the given wall temperature and the temporally averaged collision fluxes, Z_i, where i represents either CO, H_2O, CO_2, or H_2. Subsequently, the effectiveness factor is read from the precomputed table, and the average reaction rate is computed according to Eq. (4.2). To enforce the reactions on the simulated quasi-particles, the reaction probability is computed for each reactant species,

$$p_i = \langle \dot{n}_{\mathrm{r}} \rangle \, L \, A \, \frac{\nu_i}{Z_i} \,, \quad \text{for } i \in \{CO, H_2O\} \,, \quad (4.3)$$

where L and A denote the washcoat thickness and the surface area in the boundary cell, respectively. Thus, whenever a particle of type i hits the reactive boundary, this particles undergoes a reaction with probability p_i, which has to be computed beforehand in the corresponding boundary cell. For the reaction considered here, the stoichiometric coefficient, ν_i, is equal

to 1 for both reactants. This approach, on average, recovers the expected number of conversions for each reactant species. The reaction parameters are summarized in Sec. 4.2.4.

4.2.4 Washcoat parameters

Ayastuy et al. assess various different approaches to model the low temperature water-gas shift reaction [21]. In their experiments the catalyst is composed of 24.9% *CuO*, 43.7% *ZnO* and 31.4% *Al_2O_3*. The pore volume of $0.29\,\mathrm{cm}^3$ per gram catalyst implies an effective catalyst density of $2.06\,\mathrm{g/cm^3}$ considering also the pores. The predominant pore diameter in the catalyst lies between 10 and $20\,\mathrm{nm}$. The most accurate model in their study is based on the Langmuir-Hinshelwood reaction mechanism. At the temperature, $T = 453\,\mathrm{K}$, the kinetic constant for this model is $k = 1.217 \times 10^4\,\mathrm{mol/(m^3\,s\,Pa^2)}$, where the volume refers to catalyst volume. The kinetic constant is assumed to be directly proportional to the active site density. Hence lower active site densities can be mimicked by reducing k. The adsorption constants referring to the different species are:

▷ $K_{CO} = 8.562 \times 10^{-3}\,\mathrm{1/Pa}$,

▷ $K_{H_2O} = 8.898 \times 10^{-4}\,\mathrm{1/Pa}$,

▷ $K_{CO_2} = 4.581 \times 10^{-4}\,\mathrm{1/Pa}$,

▷ $K_{H_2} = 9.594 \times 10^{-4}\,\mathrm{1/Pa}$.

The geometric washcoat properties are taken from sample A15 examined by Novak et al. in [61]. Hence, the washcoat thickness is $L = 15\,\mu\mathrm{m}$. Macro- and mesoporosity if the washcoat layer are given as $\varepsilon_{\mathrm{macro}} = 0.26$ and $\varepsilon_{\mathrm{meso}} = 0.43$, respectively[2]. The pore diameter, required to compute the Knudsen diffusion coefficients in the mesopores, is assumed to be $13\,\mathrm{nm}$. The effective diffusion coefficients in the washcoat are estimated based on what Novak et al. call the "standard model" in [61]:

▷ $D_{CO}^{\mathrm{wc}} = 5.068 \times 10^{-6}\,\mathrm{m^2/s}$,

▷ $D_{H_2O}^{\mathrm{wc}} = 7.342 \times 10^{-6}\,\mathrm{m^2/s}$,

▷ $D_{CO_2}^{\mathrm{wc}} = 4.425 \times 10^{-6}\,\mathrm{m^2/s}$,

▷ $D_{H_2}^{\mathrm{wc}} = 1.553 \times 10^{-5}\,\mathrm{m^2/s}$.

---

[2] The subscripts "macro" and "meso" used in this subsection correspond to the internal structure within the washcoat layer [61]. These subscripts are not related to the macroscopic or mesoscopic scale of the multiscale study conducted in Chap. 5.

4.2.5 Bulk transport coefficients

According to [62], for the low temperature water-gas shift reaction, representative mole fractions of *CO, CO$_2$, H$_2$, N$_2$* and *H$_2$O* at the inlet are 3 %, 13 %, 30 %, 28 % and 26 %, respectively. The temperature and pressure considered are $T = 453$ K and $P = 1$ atm, respectively. The binary diffusion coefficient for each species pair can be estimated following the procedure suggested by Hirschfelder et al. in [63]. From the binary diffusion coefficients, the resulting bulk diffusion coefficients for each species in the mixture are computed as described in [64]. For the given inlet mole fractions, this approach yields:

  ▷ $D_{CO} = 5.842 \times 10^{-5}\, \text{m}^2/\text{s}$,

  ▷ $D_{H_2O} = 8.795 \times 10^{-5}\, \text{m}^2/\text{s}$,

  ▷ $D_{CO_2} = 5.225 \times 10^{-5}\, \text{m}^2/\text{s}$,

  ▷ $D_{H_2} = 1.682 \times 10^{-4}\, \text{m}^2/\text{s}$.

Note that these diffusion coefficients change with the composition of the gas mixture. Assuming that *CO* is completely consumed due to the reaction, the diffusion coefficient for *CO, H$_2$O, CO$_2$* and *H$_2$* would change by -0.9 %, $+1.2$ %, -4.2 % and 1.9 %, respectively. This effect is ignored here.

The viscosity of the gas mixture is computed according to [65]. This model requires the mass density and the viscosity of each involved component as input. The mass densities are computed from the ideal gas law. The viscosity of overheated steam is computed according to IAPWS-IF97 [66], while the dynamic viscosities of the remaining components are computed based on [67].

  ▷ $\rho_{CO} = 0.7535\, \text{kg/m}^3$, $\mu_{CO} = 2.412 \times 10^{-5}$ Pa s,

  ▷ $\rho_{H_2O} = 0.4846\, \text{kg/m}^3$, $\mu_{H_2O} = 1.537 \times 10^{-5}$ Pa s,

  ▷ $\rho_{CO_2} = 1.184\, \text{kg/m}^3$, $\mu_{CO_2} = 2.188 \times 10^{-5}$ Pa s,

  ▷ $\rho_{H_2} = 0.05423\, \text{kg/m}^3$, $\mu_{H_2} = 1.169 \times 10^{-5}$ Pa s,

  ▷ $\rho_{N_2} = 0.7536\, \text{kg/m}^3$, $\mu_{N_2} = 2.406 \times 10^{-5}$ Pa s.

For the given mole fractions, this procedure yields an average density of $\rho = 0.5298\, \text{kg/m}^3$ and an average dynamic viscosity of $\mu = 2.368 \times 10^{-5}$ Pa s. The kinematic viscosity is defined as ratio between dynamic viscosity and mass density, $\nu = \mu/\rho$.

4.2.6 Thiele modulus computation

An important dimensionless quantity for heterogeneous catalysis is the Thiele modulus, which provides information about the ratio between the time scale of diffusion and that of reaction,

$$\Phi = \sqrt{\frac{\tau_d}{\tau_r}} \, . \tag{4.4}$$

The diffusion and reaction time scale are τ_d and τ_r, respectively [60]. For large values of Φ, the mass transfer to the reactive surface is the limiting subprocess, while for small Thiele moduli the reaction rate limits the conversion [1].

Due to the abundance of H_2O in the considered system, the CO concentration is the bottleneck regarding the diffusion process. Therefore, we define the diffusion time scale τ_d as the inverse of the diffusion rate per volume at which CO is transported to the reactive surface. Assuming the reaction to be infinitely fast, i.e., zero CO at the surface, the diffusion rate per volume is given as

$$\frac{1}{\tau_d} = D_{CO} \, n_{CO,\text{in}} \, \frac{d_p{}^2}{4} \, , \tag{4.5}$$

where $n_{CO,\text{in}}$ is the number density of CO at the inlet, and $d_p/2$ denotes the pore radius of the foam structure. Analogously, τ_r is the inverse of the reaction rate per volume. Assuming instantaneous diffusion, the reaction rate per volume is given by

$$\frac{1}{\tau_r} = \dot{n}_{r,\text{in}} \, A_s \, L \, , \tag{4.6}$$

where $\dot{n}_{r,\text{in}}$ is the average reaction rate in the washcoat, as given in Eq. (4.2), for inlet conditions. A_s is the specific surface within the foam structure [14].

4.2.7 Simulation parameters

As in all mesoscopic simulation methods, the transport coefficients in iSRD depend on the spacial and temporal discretization. Moreover, in iSRD, the diffusion coefficient of a particle is directly connected to its mass: For fixed density and rotation angle, $D \propto \Delta t \, k_B T / m$ [24]. In order to avoid an additional thermostat to be necessary for the inlet-outlet boundary condition developed in Chap. 3, we choose $m_{CO,\text{sim}} = m_{CO_2,\text{sim}}$ and $m_{H_2O,\text{sim}} = m_{H_2,\text{sim}}$, which implies $D_{CO,\text{sim}} = D_{CO_2,\text{sim}}$ and $D_{H_2O,\text{sim}} = D_{H_2,\text{sim}}$. This

is expected to have minor influence on the simulation result, since the the transport away from the reactive surface is secondary.
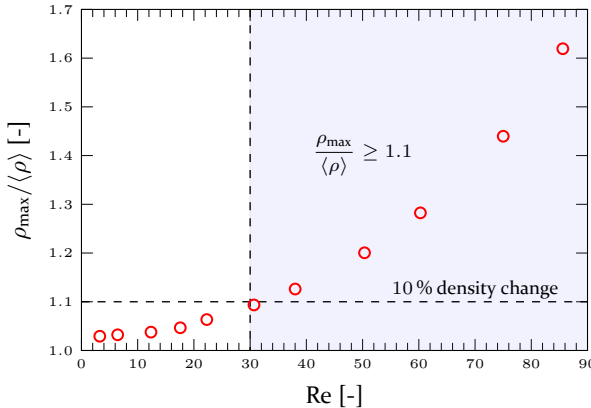
The ratio between diffusion coefficient and viscosity can be adjusted via the rotation angle and the ratio between time step and collision diameter [24]. This allows us to ensure a constant Schmidt number, $\text{Sc} = \nu/D_{CO} = 0.77$. However, for the chosen discretization, $D_{CO,\text{sim}}$ and ν_{sim} are $\sigma = 27.0$ times larger than the realistic values given in table 4.2. To compensate for that, the time scale of convective transport as well as the reaction time scale in the unit cell have to be adjusted accordingly. To this end, both the superficial velocity, U, and the effective reaction rate, $\langle \dot{n}_\text{r} \rangle$, must be increased by the same constant factor, σ. This approach ensures that, while the *dimensional* parameters chosen in the simulations may deviate from what is shown in table 4.2, all relevant *dimensionless* parameters – Reynolds number, Schmidt number and Thiele modulus – match the actual application. Note that given Reynolds and Schmidt number also the Péclet number is known. The temperature is assumed to be constant within the simulation domain. Therefore, all dimensionless numbers concerned with heat transfer play no role for the mesoscale simulations performed in this chapter.

4.3 Validation

Typical simulation results are shown in Fig. 4.8. From these results we extract the superficial velocity, U, and compute the pore size Reynolds number defined in Eq. (3.2). Further we compute the dimensionless pressure drop in form of the Hagen number,

$$\text{Hg} = -\frac{d_\text{p}{}^3}{\langle \rho \rangle \, \nu^2} \frac{dP}{dz} \, , \qquad (4.7)$$
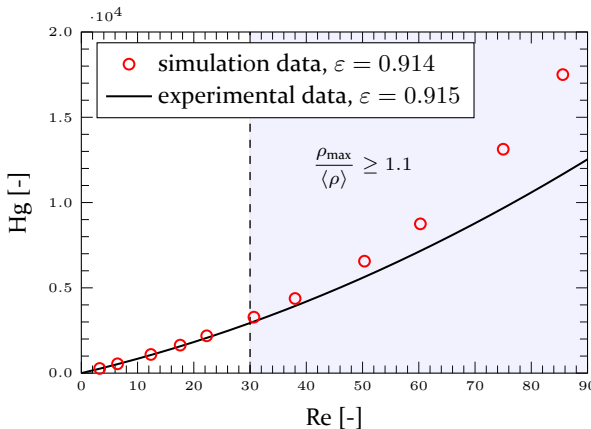
where P denotes the pressure and z is the the coordinate along the flow direction. The average mass density in the system is denoted by $\langle \rho \rangle$. In mesoscopic simulation methods [48, 25, 24], the Reynolds number can be increased either by increasing the spatial and temporal resolution or by increasing the velocity. In this study, we vary the superficial velocity, while we keep the pore size and the resolution fixed, which also fixes the kinematic viscosity. For Reynolds numbers above 30, this approach leads to density variations of more than $10\,\%$, as shown in Fig. 4.3. Since iSRD naturally includes fluctuations in density and velocity, $\rho_{\text{max}}/\langle \rho \rangle$ does not reach 1.0 as $\text{Re} \to 0$. Thus, part of the density variation depicted in Fig. 4.3 can be
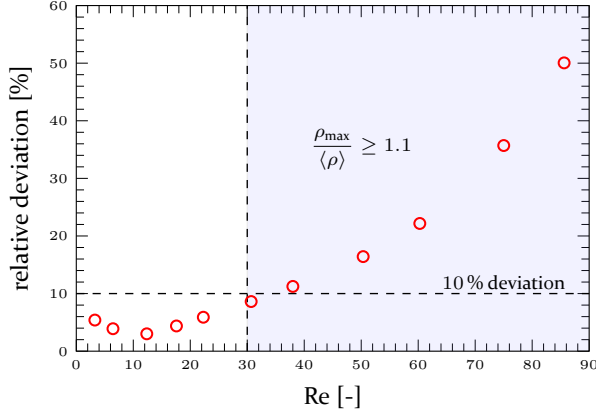
FIG. 4.3: Maximum compression within the simulation domain as a function of Reynolds number.

attributed to statistical fluctuations. To obtain the results discussed in this chapter, we average for 2×10^4 time steps, after the steady state has been reached.

In Fig. 4.4 we examine Hg as a function of Re. As shown in Fig. 4.5, below $\text{Re} = 30$, the deviations between simulation data and experimental data, taken from [23], remain below 6%. These deviations originate from the fact that the inverse sphere model cannot capture the actual foam


FIG. 4.4: We compare the relation between dimensionless pressure drop and Reynolds number in the simulations to experimental data. The experimental data used for validation refers to sample 2 in the work done by Dukhan [23].

FIG. 4.5: Relative deviation between the dimensionless pressure drop in the simulations and that in experiments.

geometry exactly. Above this point, the deviations are growing considerably with increasing Reynolds number. This growth is associated with the compressibility effects, depicted in Fig. 4.3. Hence, our model seems to give a reliable pressure drop prediction for metal foam structures in the low Reynolds number regime.

Further, we assess the mass transport to the reactive surface. In accordance to Giani et al. [6] we consider the Sherwood number over the Reynolds number in the mass transfer limited regime. Numerically, this is achieved by setting $\langle \dot{n}_r \rangle = \min(Z_{CO}, Z_{H_2O})$ in Eq. (4.3). To compare our results to the findings from [6], we need to define the effective strut size [6],

$$d_{\mathrm{s}} = d_{\mathrm{p}} \sqrt{\frac{4}{3\pi}(1 - \varepsilon)} \,, \tag{4.8}$$

as well as the strut size Reynolds number,

$$\mathrm{Re}_{\mathrm{s}} = \frac{d_{\mathrm{s}}\, U}{\nu} \,, \tag{4.9}$$
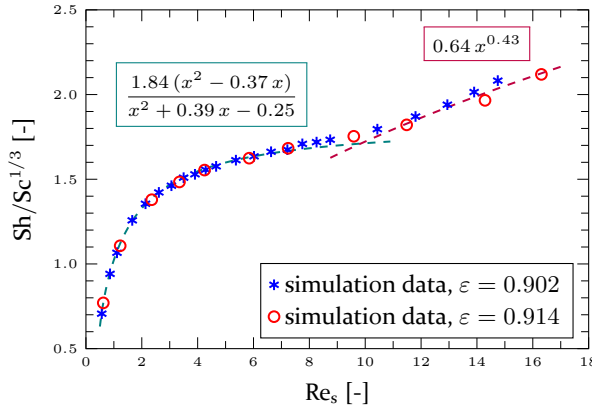
and the strut size Sherwood number,

$$\mathrm{Sh} = \frac{d_{\mathrm{s}}}{D_{CO}} \frac{-\ln(1 - \eta)}{A_{\mathrm{s}}\, h/U} \,. \tag{4.10}$$

In Eq. (4.10), the conversion, defined as

$$\eta = 1 - \frac{\dot{n}_{CO,\mathrm{out}}}{\dot{n}_{CO,\mathrm{in}}} \,, \tag{4.11}$$

53

is used. Further, h and A_s denote the unit foam cell length and the specific surface, respectively. For the two foam porosity values considered in Fig. 4.6, $Re_s \approx 0.2 \times Re$. For details, see [6, 14]. The Schmidt number, $Sc = \nu/D_{CO} = 0.77$ is kept constant in this study.
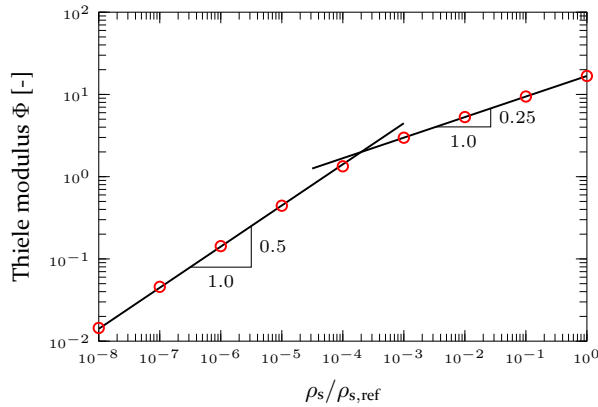

FIG. 4.6: We examine the relation between Sherwood number and Reynolds number in the simulations for two different porosity values.

Examining the relation between Sherwood and Reynolds number in Fig. 4.6, we observe two different regimes. For small Reynolds numbers, the data seems to follow a rational function, that is, the ratio between two polynomial functions. Its behavior can be explained as follows. As defined in Eq. (4.10), Sh is directly proportional to the superficial velocity, and monotonously increasing with conversion rate. Moreover, in addition to the convective transport, there is another process providing an influx of reactants, namely the diffusive transport along the main flow direction. For small superficial velocities, the conversion is mainly fed by diffusion, and the conversion hardly depends on the velocity. Therefore, increasing Re_s, which is proportional to superficial velocity, at first causes a pronounced increase in Sh. As Re_s is increased further, however, the convective transport becomes dominant, and Sh approaches a plateau. To explain this plateau, we assume that the probability for a particle to reach the reactive surface is proportional to its residence time, and therefore inversely proportional to U. Conversely, ignoring diffusion along the main flow direction, the influx of reactants is directly proportional to U. Thus, the mass transfer to the reactive surface, and with it the Sherwood number, is constant with respect to superficial velocity. This observation implies that the principal appearance of the flow

does not change significantly, but rather that the magnitude of local flow velocity simply scales with the superficial velocity.

This explanation does not hold above $Re_s \approx 10$, and before the plateau mentioned above is reached, we find a power law with the exponent reported in [6]. However, we underestimate the prefactor from Giani et al. [6] by $40\,\%$. A possible explanation for this divergence is that the considered inverse sphere packing is more regular and less tortuous compared to real foam structures.

To assess the implemented, effective reaction model, in Fig. 4.7, we investigate how the Thiele modulus, discussed in Sec. 4.2.6, changes, while increasing the active site density over the reference site density, $\rho_s/\rho_{s,\mathrm{ref}}$. For the reference site density, the reaction parameters can be found in Sec. 4.2.4. Up to a relative site density of $\rho_s/\rho_{s,\mathrm{ref}} \approx 3 \times 10^{-4}$, the Thiele modulus grows with an exponent of 0.5. Thus, the average reaction rate in the washcoat increases linearly with relative active site density, indicating that the reactions take place homogeneously within the washcoat, i.e., $\zeta \approx 1$. For higher active site densities the exponent for the increase of Φ changes to


FIG. 4.7: To assess the implemented reaction model, we are interested in the change in Thiele modulus, as the relative active site density is varied.

0.25, indicating that the effectiveness factor decreases with an exponent of 0.5, which coincides with the results shown by Roberts and Satterfield [22]. These findings indicate that our reaction model behaves correctly.

4.4 Results and Discussion
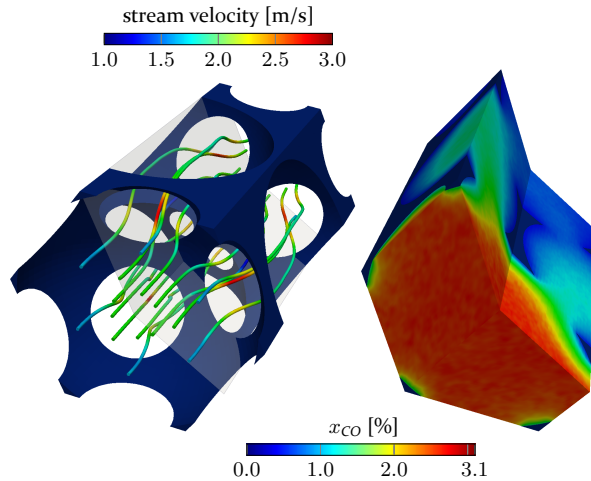
In the subsequent studies we are interested in the low Reynolds number regime. An application for this are microfluidics, where due to small system sizes, also small Thiele moduli can be observed. Therefore, we are not exclusively considering the mass transfer limited regime, but also an intermediate regime close to the reaction rate limited regime. The fluid properties of interest are summarized in Sec. 4.2.5. Details on the applied simulation setup can be found in Sec. 4.2.7.

Table 4.2: Summary of the dimensional and dimensionless parameters which are kept constant within this chapter.

dimensional		value
kinematic viscosity	ν	$4.469 \times 10^{-5}\,\mathrm{m^2/s}$
diffusion coefficient	D_{CO}	$5.842 \times 10^{-5}\,\mathrm{m^2/s}$
prism width	d_p	$0.635 \times 10^{-3}\,\mathrm{m}$
prism height	$h = \sqrt{8/3}\,d_\mathrm{p}$	$1.037 \times 10^{-3}\,\mathrm{m}$
superficial velocity	U	$1.0\,\mathrm{m/s}$
dimensionless		**value**
Reynolds number	$\mathrm{Re} = d_\mathrm{p}\,U/\nu$	14.2
Schmidt number	$\mathrm{Sc} = \nu/D_{CO}$	0.77
Péclet number	$\mathrm{Pe} = \mathrm{Re} \times \mathrm{Sc}$	10.9

To assess the influence of porosity, we consider representative foam cells. In Fig. 4.8 the flow profile and the mole fraction, x_{CO}, computed according to Eq. (3.1), are visualized for a typical simulation setup. The inlet concentration is assumed to be homogeneous over the inlet surface. The porosity will be varied by adjusting the void sphere diameter while keeping the width of the foam cell constant. Moreover, to ensure comparability, the superficial velocity is kept constant. A structure is understood to be suitable as substrate for heterogeneous catalysis, if it yields a large conversion rate, η, combined with a small pressure drop, ΔP. While η depends on the considered channel length, one can also compute an effective conversion rate, assuming an exponential profile connecting the two points $(0, \dot{n}_{CO,\mathrm{in}})$ and $(h, \dot{n}_{CO,\mathrm{out}})$. Defining an effective conversion,

$$\langle \eta \rangle = -\ln(1 - \eta)\,, \tag{4.12}$$

FIG. 4.8: We investigate the flow and concentration profile in representative unit foam cells. In this example the porosity is $\varepsilon = 0.902$. The remaining parameters are chosen according to table 4.2.

the effective exponential concentration profile along the axial coordinate, z, is given by $\dot{n}_{CO}(z) = \dot{n}_{CO,\mathrm{in}} \exp(-\langle \eta \rangle \, z/h)$.
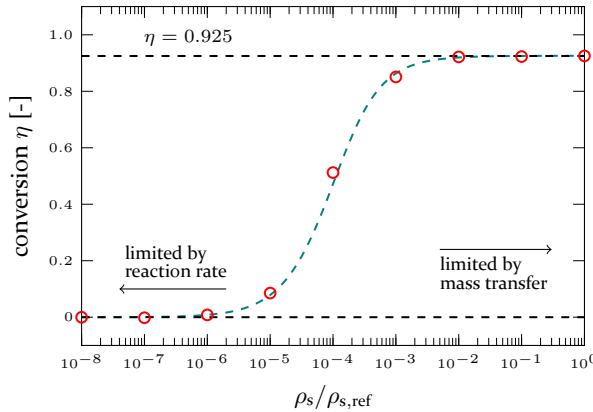
4.4.1 Active site density

Before we perform the proposed porosity study, we first characterize the regime – reaction rate limited versus mass transfer limited – which is present. To this end, we evaluate η as well as $\langle \eta \rangle$ for different active site densities.
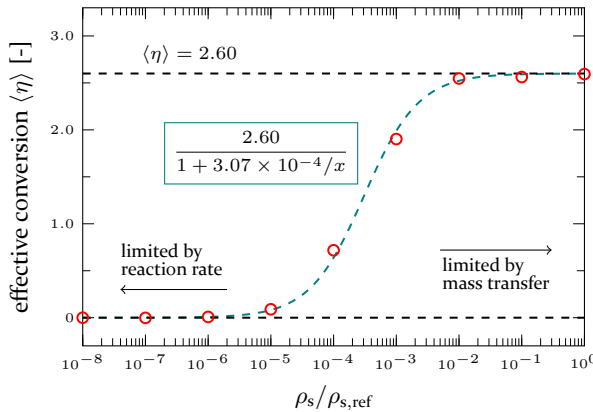
Table 4.3: Tabulation of the Thiele modulus, Φ, for the simulated values of the relative active site density, $\rho_\mathrm{s}/\rho_\mathrm{s,ref}$.

$\rho_\mathrm{s}/\rho_\mathrm{s,ref}$	10^{-8}	10^{-7}	10^{-6}	10^{-5}	10^{-4}	10^{-3}	10^{-2}	10^{-1}	10^{0}
Φ	0.0145	0.0458	0.143	0.443	1.34	2.98	5.31	9.44	16.8

As depicted in Figs. 4.9 and 4.10, the reference configuration, which is based on table 4.2, the reaction parameters found by Ayastuy et al. [21], and the washcoat properties described by Novak et al. [61], lies in the mass transfer limited regime. Starting from this reference configuration, we gradually reduce the site density to push the system towards the reaction rate limited

FIG. 4.9: For the fixed porosity value $\varepsilon = 0.902$, we vary the relative active site density in the washcoat. The dashed line is based on the fit from Fig. 4.10.

FIG. 4.10: For the fixed porosity value $\varepsilon = 0.902$, we vary the relative active site density in the washcoat. The dashed line has been fitted to the data.

regime. Table 4.3 and Fig. 4.7 show the Thiele modulus as a function of the relative site density.

Even for the rather small Reynolds and Péclet number assumed in this study, the active site density, i.e., the amount of catalyst, may be reduced by a factor of 100 compared to the reference configuration without notably reducing the conversion rate. Further, half of the maximum effective conversion is reached at a relative site density of 3.07×10^{-4}. This corresponds to $\Phi \approx 2$, which is also where the two regimes meet in Fig. 4.7. Further, note

that in the semilogarithmic axis system in Fig. 4.10, the conversion behaves similar to the sigmoid function, as the active site density is varied.

4.4.2 Porosity study
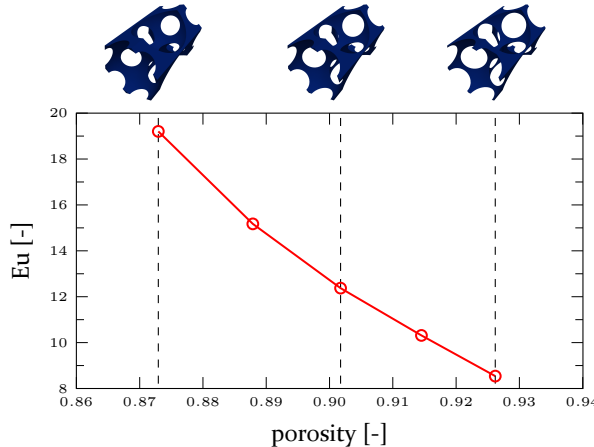
In this section we perform the aforementioned porosity study for two different active site densities:

▷ reference configuration $\qquad\rightarrow\quad \Phi = 16.8,$

▷ active sites reduced to $0.01\,\%$ $\quad\rightarrow\quad \Phi = 1.34.$

The reference configuration lies in the mass transfer limited regime, while for the other case we observe an intermediate regime, as can be seen in Figs. 4.9 and 4.10. Fig. 4.11 shows the Euler number,
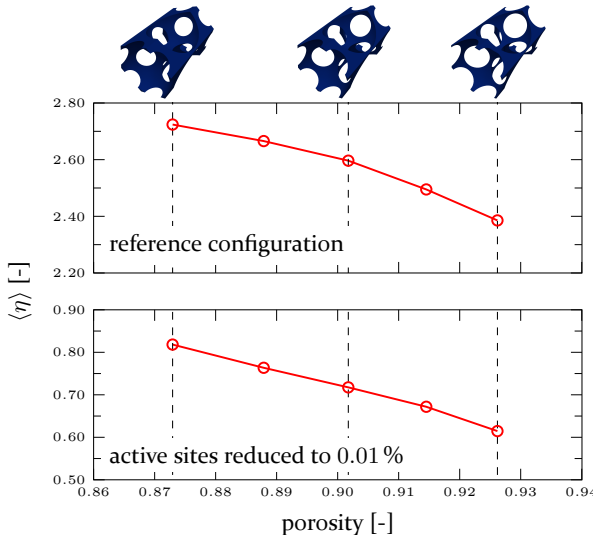
$$\text{Eu} = \frac{\Delta P}{\langle \rho \rangle\, U^2}\,, \tag{4.13}$$

as a function of foam porosity for the fixed pore size Reynolds number from table 4.2. The pressure drop along the unit foam cell is denoted as ΔP, and $\langle \rho \rangle$ is the average mass density in the system.

**FIG. 4.11:** For fixed mass flow rate, we plot the Euler number, i.e., the dimensionless pressure drop as a function of porosity. The flow resistance decreases with increasing porosity.

As Figs. 4.11 and 4.12 show, both dimensionless pressure drop and conversion rate decline, as the porosity is increased. This is expected, since with increasing porosity, the strut size as well as the reactive surface area

FIG. 4.12: For fixed mass flow rate, we plot the effective conversion rate as a function of porosity. The conversion decreases with increasing porosity.
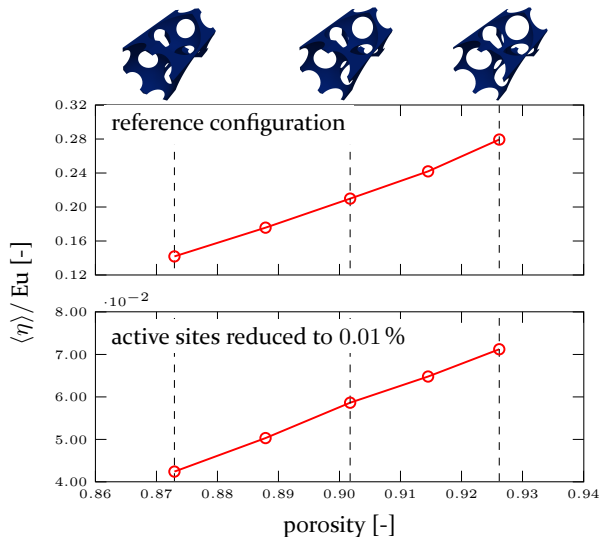
decreases. For the investigated porosity range, in the mass transfer limited regime, the effective conversion rate varies within the interval $[-8\,\%, +5\,\%]$, compared to the median, $\varepsilon = 0.902$. In the intermediate regime, the effective conversion rate varies within $[-15\,\%, +14\,\%]$. The variation is more distinctive in the intermediate regime, since there the reactants need more wall encounters on average, before the reaction finally happens.

An optimum substrate for heterogeneous catalysis should provide maximum conversion rate, while causing minimum pressure drop, ΔP. However, these two requirements cannot be fulfilled at the same time. To find a compromise, the performance index,
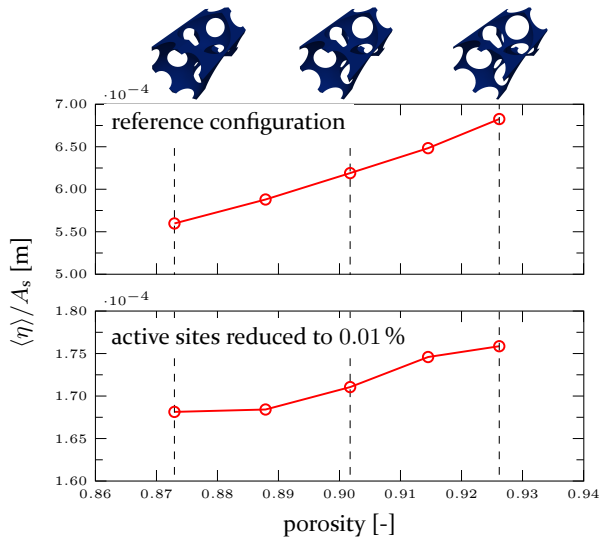
$$\text{PI} = \frac{-\ln(1-\eta)}{\Delta P/(\langle\rho\rangle\,U^2)} = \frac{\langle\eta\rangle}{\text{Eu}}\,, \tag{4.14}$$

from [6] is evaluated in Fig. 4.13 as porosity is varied. In both considered cases, the performance index monotonously increases with porosity. Note that – due to the stronger decline in $\langle\eta\rangle$ depicted in Fig. 4.10 – this increase is less distinct in the intermediate regime.
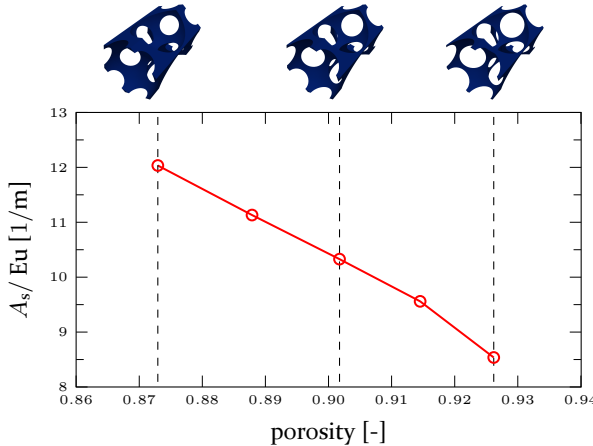
Further, the surface utilization rises with porosity, as shown in Fig. 4.14. For the specific surface, A_{s}, the analytical expression derived by Smorygo et al. [14] is used. For the same reason as above, the rise in surface utilization

**FIG. 4.13:** To evaluate the suitability for the use as substrate in heterogeneous catalysis, we consider the performance index suggested by Giani et al. in [6].


FIG. 4.14: To evaluate the surface utilization, we consider the effective conversion rate over the specific surface. In this study, the unit cell size is fixed, i.e., the actual surface area is directly proportional to the specific surface.

FIG. 4.15: To estimate the suitability for the use as substrate in heterogeneous catalysis in the reaction rate limited regime, we consider the ratio between specific surface and dimensionless pressure drop.

is less pronounced in the intermediate regime. Note that in the reaction rate limited regime, the reactants' concentration, and also $\langle \dot{n}_r \rangle$, is approximately constant throughout the system. Thus, the total reaction rate,

$$L \int_{A_r} \langle \dot{n}_r \rangle \, da \;=\; L \langle \dot{n}_r \rangle \int_{A_r} da \,, \tag{4.15}$$

where L is the washcoat layer thickness, and da denotes the surface element, is directly proportional to the available surface area, $A_r = \int_{A_r} da$. For given inlet concentrations, from the particle balance one sees that also η must be proportional to the surface area. Since η is typically small in this regime, $\langle \eta \rangle = -\ln(1-\eta) \approx \eta$. Hence, to assess the performance in the mass transfer limited regime, it is reasonable to regard the ratio between surface area and pressure drop. Following this idea, Fig. 4.15 indicates that in the reaction rate limited regime, lower porosity values are beneficial, while according to Fig. 4.13 the opposite is true in the intermediate and mass transfer limited regime.

4.5 Conclusion

In this chapter, we have combined isotropic Stochastic Rotation Dynamics with a specialized boundary condition for the inlet and outlet. Further, we have implemented and validated an effective boundary condition to model

heterogeneous catalysis at the solid walls. For small Reynolds numbers, $\text{Re} \lesssim 30$, the applied simulation approach correctly reproduces the relation between Reynolds and Hagen number from experiments [23]. Moreover, the Sherwood number obtained in the simulations behaves similar to experimental results [6]. Outside the Reynolds number range covered in the experiments, however, we have found a qualitatively different behavior. This observation indicates the transition between two different flow regimes at $\text{Re}_s \approx 10$.

Moreover, compared to the reference configuration based on [21, 61], the number of active sites may be reduced to $1\,\%$ without a significant change in conversion rate, even for the comparatively small Reynolds and Péclet number which we have considered. Beyond, we have varied the porosity keeping the pore size Reynolds number constant. In the mass transfer limited as well as intermediate regime, the surface utilization rises with increasing porosity. In agreement with the results obtained by Lucci et al. [11], we have found the performance index to rise as the porosity is increased in the mass transfer limited regime. The same trend is visible in the intermediate regime. Note that the correlation is less pronounced in the intermediate regime both with respect to surface utilization and performance index. In contrast, in the reaction rate limited regime, the obtained results indicate the surface utilization to be independent of porosity, while the performance index is expected to decrease as porosity is increased.

5 Optimum catalytic converter configuration

In this chapter, we derive a multiscale approach and derive an efficient, one-dimensional model to simulate catalytic converters filled with porous metal foam. To this end, we connect mesoscale simulations of representative unit foam cells to macroscale simulations of complete catalytic converters. The proposed approach is valid within the mass transfer limited regime. From the porosity study in Sec. 4.4.2, we pick an intermediate foam porosity, $\varepsilon = 0.902$. For the investigated foam structures, we find the performance index, defined by Giani et al. [6], to reach its maximum value, $\mathrm{PI}_{\mathrm{opt}} = 0.227$, at the Reynolds number, $\mathrm{Re}_{\mathrm{opt}} = 15.8$. The developed model is used to find optimum catalytic converter configurations for two different situations. In the first case, the heat of reaction is ignored, and one single foam segment with pore size chosen such that the Reynolds number equals $\mathrm{Re}_{\mathrm{opt}}$ is optimum. In the second case, realistic heat release values are considered leading to temperature variations along the catalytic converter. In this case, the optimum configuration consists of several, stacked foam segments with decreasing pore size along the main flow direction such that temperature fluctuations are kept small. An analytical procedure is provided to determine the optimum pore size for each segment in the stacked foam structure. Following the proposed optimisation approach, temperature variations can be eliminated, and the performance index can be increased by up to $11.0\,\%$. Moreover, the required reactive surface area, i.e., the amount of catalytic material, can be reduced by up to $18.4\,\%$.

5.1 Introduction

Catalysts are required in numerous industrial chemical processes. Therefore, to understand and optimize catalytic processes is eminently important from an economical point of view [1]. Among other geometries, open-cell metal foams are use as support structures in heterogeneous catalysis. Porous metal foam structures combine high tortuosity with large specific surface. Hence, such foam structures provide excellent mass transfer properties [5].

Conversely, the associated flow resistance is kept comparatively small due to the high porosity [6]. Various experimental and numerical studies have been performed to assess the performance of open-cell foams for heterogeneous catalysis [6, 7, 8, 11, 5, 9, 10].

However, to our knowledge, no attempt has been made to find optimum metal foam reactor designs by varying the local pore size along the main flow direction. Such an approach requires to assess catalytic converters on macroscale for numerous different pore size profiles. This is not possible in an experimental study nor is it feasible with direct numerical simulations. To address this task, we therefore conduct a multiscale approach and relate the performance of catalytic converters on macroscale to the processes within representative foam cells on mesoscale. Employing homogenization, we will develop an efficient, one-dimensional catalytic converter model. Two quantities are needed as input for the macroscale simulations: carbon monoxide conversion and pressure drop. Knowing the local pore size and temperature, the local Reynolds number can be determined. The conversion can be predicted based on the Sherwood number, which can be computed from the Reynolds number using the previously established relation depicted in Fig. 4.6. Conversely, the pressure drop can be computed from the Hagen number, which does not only depend on Reynolds number, but also on foam porosity [14]. In this chapter, the required relation between Hg and Re is established on mesoscale for the chosen porosity value. Subsequently, the developed model is applied to determine the optimum configuration for two different situations: (a) neglecting reaction heat; (b) realistic reaction heat. In the latter case, an even heat production is set as optimization goal.

5.2 Methods
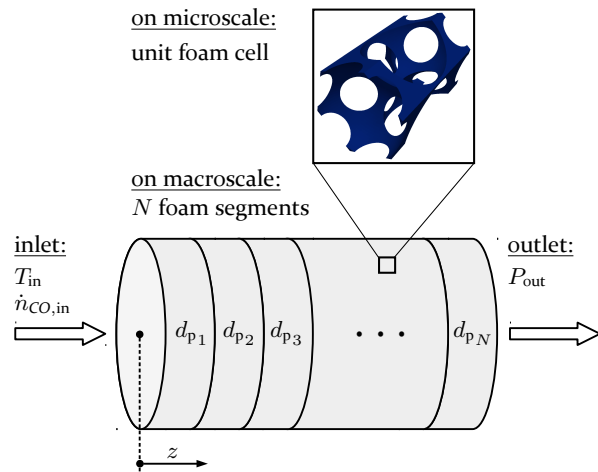
5.2.1 Model description

In this chapter, we develop a multiscale ansatz to simulate heterogeneous catalysis in foam structures. The mass transfer towards the washcoat layer is assumed to be the limiting process. As prototype reaction, we consider the low temperature water-gas shift reaction. For further details on the prototype reaction, see Chap. 4 and Sec. 5.2.2, as well as literature [21, 20, 62].

In the macroscale simulation, the foam structure within the catalytic converter is assumed to be homogeneous. For each simulation cell, we compute the local Reynolds number based on local pore size, flow velocity and temperature. Subsequently, depending on the local Reynolds number, we compute Sherwood and Hagen number from priorly established rela-

tions. Finally, we compute conversion and pressure drop in each considered simulation cell from the local Sherwood and Hagen number, respectively.

The aforementioned relations between Sh, Hg and Re have to be determined, beforehand. To this end, a representative volume element (RVE) is considered on the mesoscale. The Sherwood number depends on the Reynolds number, but not on porosity [6]. Conversely, the Hagen number is related to both the Reynolds number and the foam structure's porosity. Hence, for Sh we can use the general relation depicted in Fig. 4.6, while the relation between Hg and Re has to be determined specifically for the chosen porosity value. To this end, we employ the simulation setup introduced in Sec. 4.2.


FIG. 5.1: In the one-dimensional simulation setup for the catalytic converter, we stack foam segments with varying pore size. The temperature and *CO* influx are fixed at the inlet, while the pressure is fixed at the outlet.

In the macroscale simulation, the catalytic converter is discretized into slices along the flow direction, i.e., temperature, pore size, and consequently superficial velocity, pressure as well as *CO* content are assumed to be constant in the lateral direction. This assumption is justified as long as the heat conduction within the reactor is much faster than the heat transfer at the lateral wall.

In the simulation, for the given pore size, $d_{\mathrm{p}}(z)$, we start with an initial temperature and pressure profile as well as a constant mass flow rate, and compute mass density, superficial velocity, viscosity and *CO* diffusion coefficient. Depending on superficial velocity, U, and kinematic viscosity, ν,

from Eq. (3.2), the pore size Reynolds number is computed in each slice. For the local Reynolds number, the local Hagen number, defined in Eq. (4.7), as well as the local Sherwood number,

$$\text{Sh} = \frac{d_{\text{s}}}{D_{CO}} \frac{-\ln(1-\eta)}{A_{\text{s}}\, dz/U} = \frac{d_{\text{s}}}{D_{CO}} \frac{\langle\eta\rangle\, U}{A_{\text{s}}\, dz}\,, \tag{5.1}$$

are computed using the previously established relations. In the definition of Sh, the effective strut diameter, d_{s}, defined in Eq. (4.8), and the carbon monoxide conversion, η, from Eq. (4.11) are used. D_{CO} is the diffusion coefficient associated with carbon monoxide. A_{s} is the specific surface, while dz denotes the spatial resolution, i.e., the width of the considered slice. From Eqs. (4.7) and (5.1), the pressure drop and the *CO* conversion in each slice along the catalytic converter are computed as

$$dP = \frac{\rho\, \nu^2}{d_{\text{p}}{}^3}\,\text{Hg}\, dz\,, \tag{5.2}$$

and

$$\eta = 1 - \exp\left(A_{\text{s}}\, \frac{D_{CO}}{d_{\text{s}}}\, \frac{dz}{U}\, \text{Sh} \right)\,, \tag{5.3}$$

respectively. Since Eq. (5.2) is formulated on macroscale, the macroscopic mass density, ρ, is used[1].

The *CO* conversion is related to the decline in the ratio between *CO* and total particle flux, C_{CO}, along the catalytic converter. The formal definition of C_{CO} is provided in Eq. (3.3). Throughout this chapter, we will use the abbreviation $C := C_{CO}$. For brevity, this quantity will be referred to as *CO* fraction. For a given conversion, the relative decline of the *CO* fraction is $\delta C = 1 - \eta$. Knowing the pressure drop values, for the assumed pressure at the outlet, the pressure profile in the reactor is computed. Knowing the *CO* consumption, the reaction rate and the heat release in each volume element can be calculated. The reaction rate is computed by balancing the convective and diffusive particle transport into and out of each simulated slice. The heat release from the reaction as well as the convective heat transport is used as input, in order to update the temperature profile performing one time step

---

[1] Note that in contrast to the macroscopic mass density, the mesoscopic mass density is superimposed by fluctuations. Hence, in Eq. (4.7), which is formulated on mesoscale, the average value of the fluctuating, mesoscopic density, $\langle\rho\rangle$, is used. The symbols $\langle\rho\rangle$ and $\rho_{\max}$ denote the average and maximum density on mesoscale, respectively. Conversely, whenever we use the greek letter ρ without brackets or subscript, the macroscopic density field is addressed.

with the finite volume method. The time step is given by $dt = 0.5\,dz/U_0$, where U_0 is the superficial at $1\,\text{atm}$ and $453\,\text{K}$. This cycle is repeated until the temporal variations in all quantities vanish.

As shown in Fig. 5.1, the macroscale simulation model allows for stacking numerous foam segments[2], $j \in \{1,..,N\}$, with varying pore size, d_{p_j}. Throughout this chapter, the outlet pressure is fixed to $1\,\text{atm}$. For inlet temperature and *CO* fraction, the values $453\,\text{K}$ and $3.0\,\%$ are used, respectively. Moreover, the mass flow rate, $\dot{m}$, as well as the heat transfer coefficient at the lateral wall, α, have to be prescribed. Using d_{p_j} as design variables, we can determine optimum configurations with respect to different objectives.

5.2.2 Gas and foam properties

As in Chap. 4, we consider the low temperature water-gas shift reaction as prototype reaction. The mole fractions of *CO*, CO_2, H_2, N_2 and H_2O at the inlet are chosen as $3\,\%$, $13\,\%$, $30\,\%$, $28\,\%$ and $26\,\%$, respectively [62]. We assume the mass transfer towards the washcoat to be the rate limiting process. Moreover, due to the abundance of H_2O, the model is valid for (quasi-) first order reactions. Following the procedure from Sec. 4.2.5, The viscosity and the diffusion coefficients are computed depending on temperature [65, 66, 63, 64]. In Fig. 5.2 we show the actual viscosity
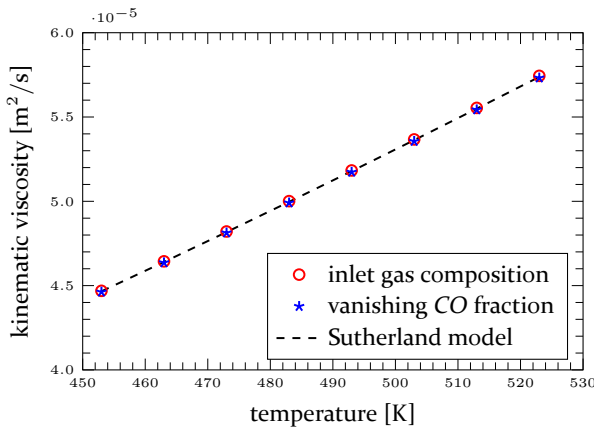

FIG. 5.2: Kinematic viscosity, ν, of the gas mixture as a function of temperature.

---

[2] Throughout this chapter, the term "segment" denotes cylindrical foam pieces. Conversely, the term "slice" addresses the numerical discretization of the macroscopic simulation domain. Note that each segment must comprise at least one slice.
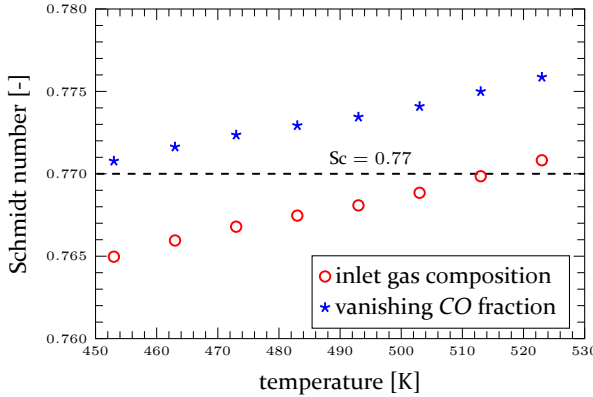
FIG. 5.3: Schmidt number, $Sc = \nu/D_{CO}$, as a function of temperature.

depending on the gas composition compared to the employed Sutherland model,

$$\nu = \frac{1}{\rho} \frac{C_S \sqrt{T}}{1 + T_S/T},\tag{5.4}$$

where $C_S = 1.497 \times 10^{-6}\,\mathrm{kg/(m\,s\,\sqrt{K})}$ and $T_S = 157\,\mathrm{K}$. The mass density, ρ, is computed from the ideal gas law. For the inlet gas composition, the Sutherland model underestimates the viscosity by roughly 0.1%, while for vanishing *CO* fraction, the viscosity is overestimated by approximately 0.1%. Moreover, Fig. 5.3 shows the Schmidt number as a function of temperature. In the simulations, we fix the Schmidt number to $Sc = 0.77$. The maximum deviations in the considered temperature range are below $0.8\,\%$. The specific heat is assumed to be independent of temperature. The values used in the simulation correspond to $T = 450\,\mathrm{K}$:

> $\triangleright$ $c_{p,CO} = 1.054 \times 10^3\,\mathrm{J/(kg\,K)}$,
>
> $\triangleright$ $c_{p,H_2O} = 1.926 \times 10^3\,\mathrm{J/(kg\,K)}$,
>
> $\triangleright$ $c_{p,CO_2} = 0.978 \times 10^3\,\mathrm{J/(kg\,K)}$,
>
> $\triangleright$ $c_{p,H_2} = 14.50 \times 10^3\,\mathrm{J/(kg\,K)}$,
>
> $\triangleright$ $c_{p,N_2} = 1.049 \times 10^3\,\mathrm{J/(kg\,K)}$.

The foam structure is assumed to consist of aluminum with density, $\rho_{Al} = 2.70 \times 10^3\,\mathrm{kg/m^3}$, and specific heat capacity, $c_{p,Al} = 0.897 \times 10^3\,\mathrm{J/(kg\,K)}$. The geometric foam properties are computed for an inverse sphere packing with constant porosity, $\varepsilon = 0.902$ [14]. Further, the heat conduction in

the gas phase is ignored, i.e., the effective thermal conductivity is given by $(1 - \varepsilon)\, k_{Al}$. The thermal conductivity of aluminum is assumed to be constant, $k_{Al} = 235\,\mathrm{W}/(\mathrm{m\,K})$. The effective diffusion coefficient of *CO* is computed as $D_{\mathrm{eff},CO} = \varepsilon\, D_{CO}$, where D_{CO} denotes the bulk diffusion coefficient of carbon monoxide. The remaining simulation parameters are chosen as in Sec. 4.2.

5.3 Results and Discussion

5.3.1 Pressure drop prediction

To examine the pressure drop in a representative volume element, we employ the simulation software developed and validated in [13, 24] and Chaps. 3 and 4. The foam structure is modeled as an inverse sphere packing, which can be fully described by two parameters: the distance between the sphere centers, which is the same as the pore size, d_{p}, and the sphere diameter, d. The ratio between sphere diameter and distance is denoted as $k = d/d_{\mathrm{p}}$. In the relevant parameter range there is a one-to-one correspondence between k and porosity, ε. For inverse sphere packings, Smorygo et al. derive a specified version of the Forchheimer equation [14],
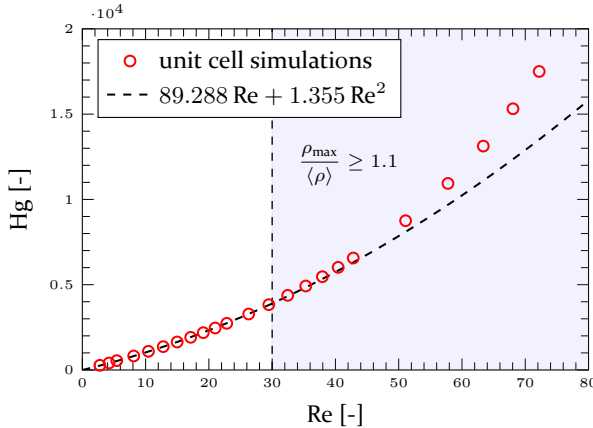
$$\frac{1}{\rho}\frac{dP}{dz} = A\,\frac{A_{\mathrm{s}}^2}{\varepsilon^3}\,\nu\,U + B\,\frac{A_{\mathrm{s}}}{\varepsilon^3}\,U^2\,,\tag{5.5}$$

where A and B are fit parameters. Specific surface and porosity are defined as $A_{\mathrm{s}} = f(k)/d_{\mathrm{p}}$ and $\varepsilon = g(k)$, respectively, where $f(k)$ and $g(k)$ are known functions [14]. Exploiting Eqs. (3.2) and (4.7), Eq. (5.5) can be written as

$$\mathrm{Hg} = a\,\mathrm{Re} + b\,\mathrm{Re}^2\,,\tag{5.6}$$

where $a = A\, f(k)^2/g(k)^3$ and $b = B\, f(k)/g(k)^3$ depend only on k. Throughout this chapter, we use $k = 1.090$, fixing the porosity to $\varepsilon = 0.902$ [14].

From simulations for the representative unit foam cell on mesoscale as described in Sec. 4.2, we can determine the relation between Hg and Re for the given porosity value. The results are depicted in Fig. 5.4. Given the pore size, viscosity and mass density, knowing the Hagen number is sufficient to predict the pressure gradient in the macroscale simulation. Similarly, the *CO* consumption can be extracted from the Sherwood number.

FIG. 5.4: For the chosen porosity value, we determine the Hagen number as a function of pore size Reynolds number. Density variations due to compressibility are overestimated in the simulations. To keep errors small, the fit is computed for Re $\in [0, 30]$, where the maximum compression in the simulation, $\rho_{\max}/\langle\rho\rangle - 1$, is below $10\,\%$, see Sec. 4.3.
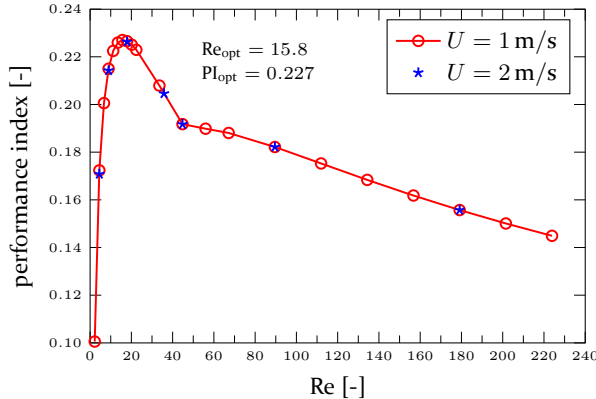
5.3.2 Optimum – negligible heat release

In this section we determine the optimum configuration in case heat production is negligible, and the temperature can be assumed to be constant along the catalytic converter.

An important quantity to characterize the performance of support structures used for heterogeneous catalysis is the performance index [6]. Inserting Eqs. (3.2), (4.7) and (5.1) into Eq. (4.14) yields the relation,

$$\mathrm{PI} = h(k)\,\frac{\mathrm{Sh}}{\mathrm{Hg}}\,\frac{\mathrm{Re}}{\mathrm{Sc}}\,,\tag{5.7}$$

where $h(k)$ is a known function. As mentioned above, the Schmidt number, $\mathrm{Sc} = 0.77$, is kept constant throughout this study. Further details on the simulation parameters are provided in Sec. 5.2.2. Since local Sherwood and Hagen number are fully determined by local Reynolds number and porosity, the same is true for the local performance index. In Fig. 5.5, we plot the relation between performance index and Reynolds number for the considered porosity value. The maximum performance index, $\mathrm{PI}_{\mathrm{opt}} = 0.227$, is reached at $\mathrm{Re}_{\mathrm{opt}} = 15.8$. The two regimes visible in Fig. 5.5 correspond to the two regimes found for the relation between Sh and Re plotted in Fig. 4.6.
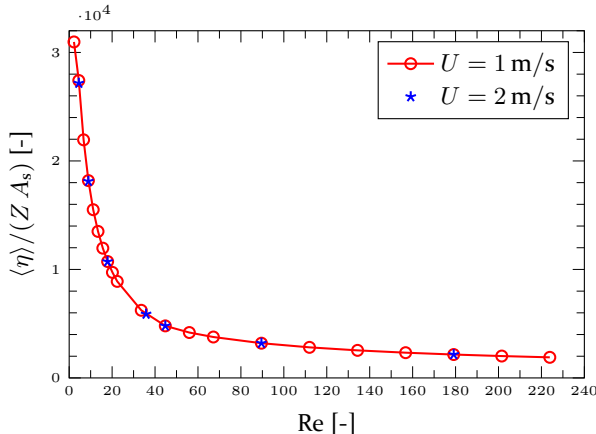
FIG. 5.5: Performance index as a function of pore size Reynolds number for the foam porosity value $\varepsilon = 0.902$.

Further, using the definition from Eq. (4.12), the effective conversion per reactor length, Z, and specific surface area, A_s, is given as

$$\frac{-\ln(1 - \eta)}{Z\,A_s} = \frac{\langle \eta \rangle}{Z\,A_s} = \frac{1}{l(k)}\frac{\mathrm{Sh}}{\mathrm{Re}\,\mathrm{Sc}}\,, \tag{5.8}$$

where $l(k)$ is again some known function. As shown in Fig. 5.6, the surface exploitation in the unit foam cell reaches its maximum at vanishing Reynolds number.


FIG. 5.6: Surface exploitation as a function of pore size Reynolds number for the foam porosity value $\varepsilon = 0.902$.
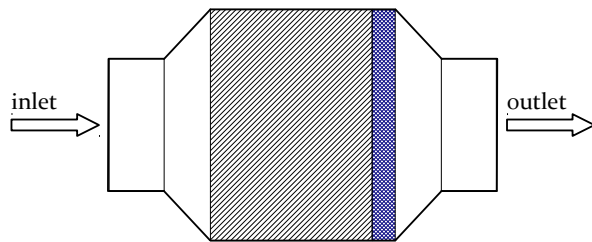
The presented multiscale model allows for assembling a catalytic converter on macroscale consisting of segments with possibly different pore sizes. In each slice, i, of the macroscale simulation domain, the pressure drop, dP_i, and the relative change in the *CO* fraction, δC_i, are computed. Consequently, inlet pressure and outlet *CO* fraction are given by

$$P_{\text{in}} = P_{\text{out}} + \sum_{i \in \text{slices}} dP_i = P_{\text{out}} + \Delta P \qquad (5.9)$$

and

$$C_{\text{out}} = C_{\text{in}} \times \prod_{i \in \text{slices}} \delta C_i = C_{\text{in}} \times (1 - \eta_{\text{tot}}) , \qquad (5.10)$$

respectively. As long as temperature variations are small, dP_i and δC_i do not depend on the position of the slice, i. Since both addition and multiplication are commutative, P_{in}, C_{out}, and, consequently, the performance index do not depend on the segment arrangement. Hence, there is no reason for stacking


FIG. 5.7: This setup is suggested as optimum in case the heat of reaction is ignored. The reactions occur in the thin slice on the right, filled with fine-pored foam. The coarse-pored foam element on the left does not need any washcoat, since its primary purpose is to ensure homogeneous flow conditions at the contact area between the two foam segments.

segments of different pore size. Conversely, tho optimum configuration consists of just one single segment. The pore size in this segment is adjusted so that the optimum Reynolds number is obtained. As shown in Fig. 5.7, another segment with rather coarse-pored foam, which is not necessarily washtcoated, might be slotted in ahead, in order to generate homogeneous flow conditions. Note that at Re_{opt}, not only the performance index is maximum, but also the surface exploitation is high.

5.3.3 Optimum – realistic heat release

Even weakly exothermic reactions, such as the low temperature water-gas shift reaction, are able to cause significant temperature variations within a

catalytic converter. However, the pore size can be adjusted such that an even reaction rate, and therefore even heat release, is obtained along the reactor. In this section, we present a simple recipe to determine the pore size, $d_\mathrm{p}(z)$, such that temperature fluctuations in the reactor are minimum. To this end, we assume the relation $\mathrm{Sh} = \psi\,\mathrm{Re_s^{0.43}}\,\mathrm{Sc}^{1/3}$ to be valid, i.e.,

$$\mathrm{Re_s} = \frac{d_\mathrm{s}\,U}{\nu} \gtrsim 10 \quad \Leftrightarrow \quad \mathrm{Re} = \frac{d_\mathrm{p}\,U}{\nu} \gtrsim 50\,. \tag{5.11}$$

In numerical simulations of inverse sphere packings, $\psi = 0.64$ has been found in Sec. 4.3, while in experimental studies of real metal foam, which is more irregular, $\psi = 1.1$ has been observed [6].

Inserting Eq. (5.1) and the definition of the Schmidt number yields a relation for the required strut size Reynolds number in each segment, j,

$$\left[\,\mathrm{Re_s}\,\right]_j = \left(\frac{\psi}{\mathrm{Sc}^{2/3}} \left[\frac{A_\mathrm{s}\,\Delta z}{-\ln(1-\eta)} \right]_j \right)^{1.75}, \tag{5.12}$$

depending on the width, Δz, of the segment and the conversion, η, along the segment. Note that the right hand side depends on the pore size via A_s. Exploiting that
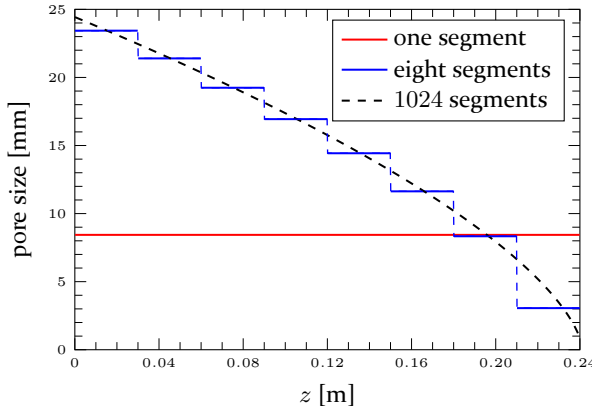
$$(A_\mathrm{s} \times d_\mathrm{p}) = \sqrt{2}\pi k(6 - 5k) \tag{5.13}$$

is independent of d_p [14], we find an explicit relation for the pore size in each segment,

$$d_{\mathrm{p}j} = \left[\frac{\nu_j}{U_j} \sqrt{\frac{3\pi}{4(1-\varepsilon)}} \left(\frac{\psi}{\mathrm{Sc}^{2/3}} \frac{(A_\mathrm{s} \times d_\mathrm{p})\,\Delta z_j}{-\ln(1-\eta_j)} \right)^{1.75} \right]^{1/2.75}, \tag{5.14}$$
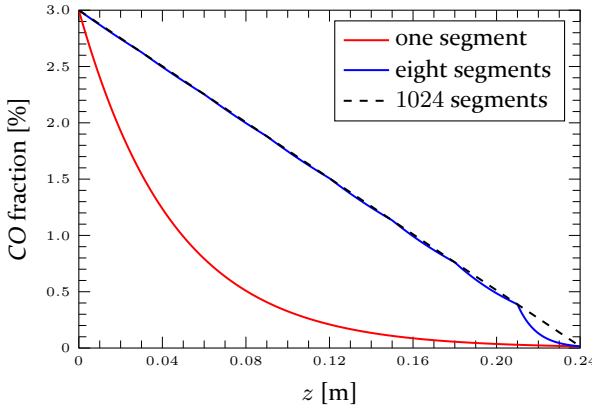
which achieves a requested carbon monoxide conversion, η_j. Through U_j and ν_j, $d_{\mathrm{p}j}$ depends on the temperature in the segment. To obtain an even reaction rate, the conversion, η_j, is chosen such that the absolute change in *CO* fraction is equal in each segment.

We apply this concept to a cylindrical catalytic converter with length and radius of $0.24\,\mathrm{m}$ and $4.49 \times 10^{-2}\,\mathrm{m}$, respectively. The converter is filled with metal foam modeled as an inverse sphere packing, i.e., $\psi = 0.64$. The superficial velocity is $U = 2\,\mathrm{m/s}$ and the requested total conversion is $\eta_\mathrm{tot} = 99.5\,\%$. The heat transfer coefficient at the lateral wall is assumed as $\alpha = 120\,\mathrm{W/K\,m^2}$. The inlet temperature is $453\,\mathrm{K}$, while the temperature at the wall is chosen as $403\,\mathrm{K}$. Note that the simulation parameters have been adjusted such that for the $50\,\mathrm{K}$ temperature difference, the heat removed
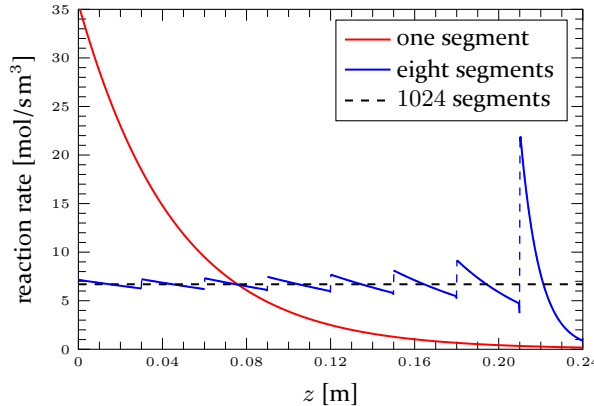
FIG. 5.8: For three different segment numbers, we plot the pore size, d_{p_j}, computed according to Eq. (5.14), aiming for an even reaction rate along the catalytic converter.

at the lateral wall is equal to the heat released in the reaction. Fig. 5.8 shows the pore size determined according to Eq. (5.14) as function of z for different segment numbers. As depicted in Fig. 5.9, the carbon monoxide
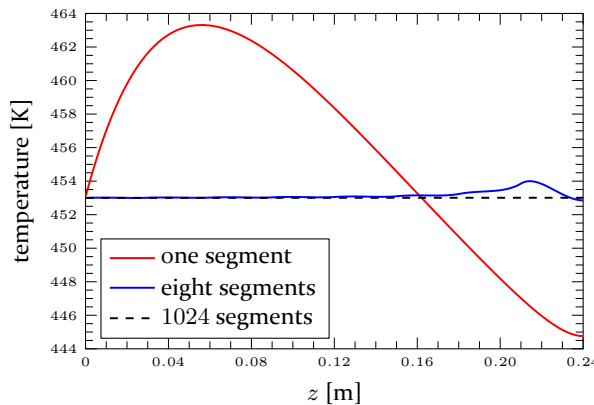

FIG. 5.9: For three different segment numbers, we plot the carbon monoxide fraction as a function of position within the catalytic converter.

content drops exponentially in each segment. The more segments we use, i.e., the smaller the segment length, the closer the *CO* fraction profile to a linear decrease. Accordingly, the reaction rate shown in Fig. 5.10, which is computed from the *CO* fraction profile, converges to a constant value when increasing the number of segments. The temperature variations in

FIG. 5.10: For three different segment numbers, we plot the reaction rate, which governs the heat release, as a function of position within the catalytic converter.


FIG. 5.11: For three different segment numbers, we plot the temperature as a function of position within the catalytic converter.

Fig. 5.11 are caused by the deviations from the horizontal line of constant reaction rate in Fig. 5.10, and consequently by the deviation from the linear *CO* fraction profile in Fig. 5.9. The total temperature difference within the catalytic converter decreases as the number of segments is increased.

In Figs. 5.12 to 5.14, we plot the total temperature variation within the reactor, the total performance index and the required active surface, respectively. For the examined system, using four segments instead of one reduces the temperature range within the converter from $18.6\,\mathrm{K}$ to $3.3\,\mathrm{K}$. Moreover, using four segments reduces the necessary reactive area by $12.4\,\%$, while
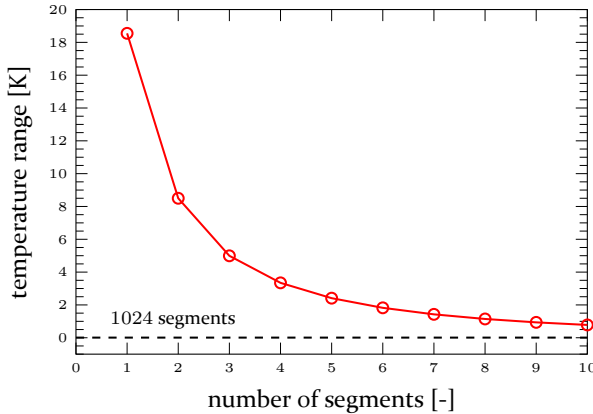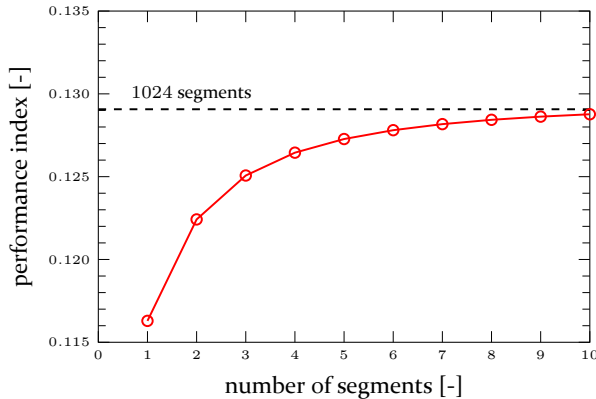
FIG. 5.12: Temperature fluctuations as a function of the number of segments.

increasing the total performance index by 8.7%. Increasing the number of segments further leads to a vanishing temperature range. Compared to the single segment setup, 18.4% of the required reactive area can be saved, and the performance index can be increased by up to 11.0%. Note that in the considered situation, the conversion is fixed, i.e., an increase in the performance index is equivalent to a decrease in the pressure drop along the converter.
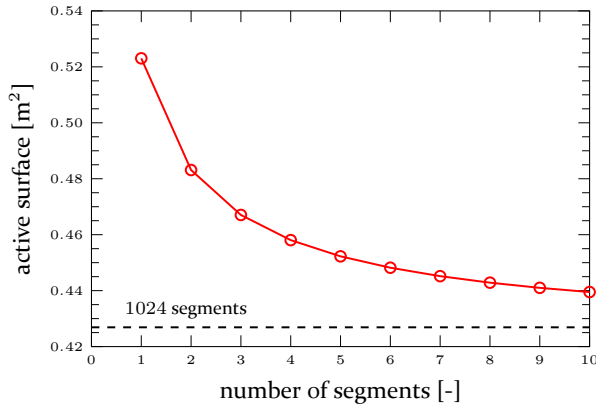
5.4 Conclusion

In this chapter, we have developed a simulation tool for heterogeneous catalysis in open-cell metal foam. To this end, we have conducted a multi-scale approach connecting the detailed representation of foam structures on mesoscale to an effective model for catalytic converters on macroscale. In the macroscale simulations, the foam structure has been taken into account based on relations between pore size Reynolds number and Hagen as well as Sherwood number, which have been established on mesoscale beforehand.

Moreover, we have developed simple recipes to determine the optimum pore size profile within a catalytic converter for two different cases. In the first case, the heat of reaction is ignored, while in the second case, the heat release due to reactions within the catalytic converter is considered. In the latter, more realistic case, adjusting the pore size along the main flow direction has been found to significantly improve the converter's performance. To demonstrate this, we have compared different catalytic converters consisting

FIG. 5.13: Performance index as a function of the number of segments.

FIG. 5.14: Total active surface required as a function of the number of segments.

of one or more foam segments. The constant pore size within each segment is computed following the developed optimization recipe. The configuration which comprises one single foam segment serves as reference. For fixed conversion and converter size, we have found that stacking just four segments with different pore sizes, already reduces temperature fluctuations and pressure losses along the converter substantially. Additionally, the active surface area required in the converter, which is proportional to the required amount of catalytic substances, is decreased considerably. Thus, applied in chemical industry, the proposed optimization procedure has the potential to reduce the costs associated with maintaining pressure drops as well as providing catalytic materials.

6 Conclusion and outlook

6.1 Conclusion

In this work, we have modified Stochastic Rotation Dynamics to obtain a mesoscopic simulation method which is isotropic by construction. This method, Isotropic Stochastic Rotation Dynamics, allows us to model gas dynamics in porous foam structures without introducing anisotropies at the complex shaped boundaries. We have, further, developed specialized open boundaries for particle-based simulations of reactive flows, to treat the inlet and outlet boundary conditions in unit foam cell simulations, correctly. The chemical reactions have been assumed to take place within a porous washcoat layer, which has not been simulated explicitly. Instead, an effective reaction model has been applied bases on precomputed values for the effectiveness factor associated to the washcoat layer. This reaction model has been adapted to the low temperature water-gas shift reaction, which has been assumed to follow the Langmuir-Hinshelwood reaction mechanism [21].

To validate the implemented simulation, we have assessed the relation between Hagen and Reynolds number as well as the relation between Sherwood and Reynolds number, within the representative unit foam cell. The obtained simulation results for the Hagen number agree with experimental findings, especially at low Reynolds numbers [23]. Moreover, within the parameter range covered in the experiments, the Sherwood number observed in the simulations behaves similar to the experimental data [6]. For smaller Reynolds numbers, however, we find a qualitatively different behavior, indicating the transition between two different flow regimes at the strut size Reynolds number, $Re_s \approx 10$.

Further, we have assessed the unit foam cell's performance as support structure for heterogeneous catalysis at different porosity values. For the considered pore size Reynolds number, $Re = 14.2$, the surface utilization improves as the porosity is increased, both in the mass transfer limited and in the intermediate regime. In accordance to [11], we find that the performance

index rises with increasing porosity in the mass transfer limited regime. The same is true in the intermediate regime, however, as for the surface utilization, the effect is less pronounced. Conversely, in the reaction rate limited regime, the surface utilization is expected to stay constant, while the performance index should even decline as the porosity is increased.

In addition, we have conducted a multiscale approach to develop a simulation tool for macroscopic catalytic converters filled with metal foam. On the macroscale, the foam structure has not been simulated explicitly, but it has been modeled effectively through relations between pore size Reynolds number and Hagen as well as Sherwood number. These relations have been established on the mesoscale, beforehand. Using the developed macroscale model for the fixed foam porosity value, $\varepsilon = 0.902$, the trade-off between conversion and pressure drop has been found to be optimum at pore size Reynolds number, Re $= 15.8$.

Furthermore, we have used the developed macroscale model to find optimum catalytic converter configurations. To this end, we have distinguished between two different situations. The first one addresses the idealized case in which the heat of reaction is ignored. Conversely, the second one covers the realistic case in which the reaction heat has significant effect on the processes within the catalytic converter. For both cases, we have presented a simple recipe to determine the optimum pore size configuration within the catalytic converter. In the latter, more interesting case, we have shown that adjusting the pore size within the converter can substantially improve the performance. Compared to the configuration with constant pore size along the complete catalytic converter, stacking four segments with each having constant pore size, already results in a significant reduction of temperature fluctuations and pressure losses along the converter. Moreover, associated with the active surface area, the amount of catalytic substances required in the converter can be decreased substantially. This result has high economical relevance, since it enables the chemical industry to perform catalytic processes at controlled temperatures and at lower costs, which typically originate from maintaining necessary pressure drops and from providing expensive catalytic materials.

6.2   Outlook

Based on the achievements presented in this thesis, the next step could be to build real catalytic converters according to the developed recipes, and to investigate their behavior in experiment. This would allow us to assess the

validity of the implemented model. If necessary, it could serve as the basis for possible improvements in the model. If experiments can substantiate the findings presented here, the way will be paved for an industrial application of the suggested optimization approach.

Note that the developed simulation tool is not restricted to foam structures. The presented multiscale approach is applicable to heterogeneous catalysis in any geometric structure which can be described by one or more representative volume elements on the mesoscale. Together with the complex shapes which can be produced by 3D printing, for example, the presented model enables us to further develop and optimize innovative support structures for heterogeneous catalysis.

Beyond, the mesoscale simulation software described in Chap. 4 has numerous further applications. For example, additional reaction mechanisms can be easily added to the model, allowing for the investigation of further processes, such as chromatography in porous media. Another interesting project feasible with the developed software concerns the characterization of the dispersion coefficient, which plays an important role in reactor design, for foam structures and porous media in general.

Bibliography

[1] O. Deutschmann, H. Knözinger, K. Kochloefl, and T. Turek. *Heterogeneous Catalysis and Solid Catalysts*. Wiley, New York, 2009.

[2] P. Atkins and J. de Paula. *Atkins' Physical Chemistry*. Oxford University Press, New York, 2010.

[3] J.M. Winterbottom and M. King. *Reactor Design for Chemical Engineers*. Taylor & Francis, 1999.

[4] M. V. Twigg and J. T. Richardson. Theory and applications of ceramic foam catalysts. *Chemical Engineering Research and Design*, 80:183–189, 2002.

[5] F. Lucci, A. Della Torre, G. Montenegro, and P. Dimopoulos Eggenschwiler. On the catalytic performance of open cell structures versus honeycombs. *Chemical Engineering Journal*, 264:514–521, 2015.

[6] L. Giani, G. Groppi, and E. Tronconi. Mass-transfer characterization of metallic foams as supports for structured catalysts. *Industrial & Engineering Chemistry Research*, 44:4993–5002, 2005.

[7] G. Groppi, L. Giani, and E. Tronconi. Generalized correlation for gas/solid mass-transfer coefficients in metallic and ceramic foams. *Industrial & Engineering Chemistry Research*, 46:3955–3958, 2007.

[8] S. T. Kolaczkowski, S. Awdry, T. Smith, D. Thomas, L. Torkuhl, and R. Kolvenbach. Potential for metal foams to act as structured catalyst supports in fixed-bed reactors. *Catalysis Today*, 273:221–233, 2016.

[9] J. von Rickenbach, F. Lucci, C. Narayanan, P. Dimopoulos Eggenschwiler, and D. Poulikakos. Multi-scale modelling of mass transfer limited heterogeneous reactions in open cell foams. *International Journal of Heat and Mass Transfer*, 75:337–346, 2014.

[10] J. von Rickenbach, F. Lucci, P. Dimopoulos Eggenschwiler, and D. Poulikakos. Pore scale modeling of cold-start emissions in foam based catalytic reactors. *Chemical Engineering Science*, 138:446–456, 2015.

[11] F. Lucci, A. Della Torre, J. von Rickenbach, G. Montenegro, D. Poulikakos, and P. Dimopoulos Eggenschwiler. Performance of randomized Kelvin cell structures as catalytic substrates: Mass-transfer based analysis. *Chemical Engineering Science*, 112:143–151, 2014.

[12] C. S. Peskin. The immersed boundary method. *Acta Numerica*, 11:479–517, 2002.

[13] S. Strobl. *Mesoscopic Particle-based Fluid Dynamics in Complex Geometries*. PhD thesis, Friedrich-Alexander-Universität Erlangen-Nürnberg, 2017.

[14] O. Smorygo, V. Mikutski, A. Marukovich, A. Ilyushchanka, V. Sadykov, and A. Smirnova. An inverted spherical model of an open-cell foam structure. *Acta Materialia*, 59:2669–2678, 2011.

[15] C. M. Hoffmann. *Geometric and Solid Modeling: An Introduction*. Morgan Kaufmann Publishers, San Francisco, 1989.

[16] G.A. Bird. *Molecular Gas Dynamics and the Direct Simulation of Gas Flows*. Molecular Gas Dynamics and the Direct Simulation of Gas Flows. Clarendon Press, 1994.

[17] G. A. Bird. Perception of numerical methods in rarefied gas dynamics. *Progress in Astronautics and Aeronautics*, 117:211–226, 1989.

[18] A. Malevanets and R. Kapral. Mesoscopic model for solvent dynamics. *Journal of Chemical Physics*, 110:8605–8613, 1999.

[19] M. Wang and Z. Li. Simulations for gas flows in microgeometries using the direct simulation Monte Carlo method. *International Journal of Heat and Fluid Flow*, 25:975–985, 2004.

[20] I. Fishtik and R. Datta. A UBI-QEP microkinetic model for the water-gas shift reaction on Cu(111). *Surface Science*, 512:229–254, 2002.

[21] J. L. Ayastuy, M. A. Gutiérrez-Ortiz, J. A. González-Marcos, A. Aranzabal, and J. R. González-Velasco. Kinetics of the low-temperature WGS reaction over a CuO/ZnO/Al2O3 catalyst. *Industrial & Engineering Chemistry Research*, 44:41–50, 2005.

[22] G. W. Roberts and C. N. Satterfield. Effectiveness factor for porous catalysts. Langmuir-Hinshelwood kinetic expressions for bimolecular surface reactions. *Industrial & Engineering Chemistry Fundamentals*, 5:317–325, 1966.

[23] N. Dukhan. Correlations for the pressure drop for flow through metal foam. *Experiments in Fluids*, 41:665–672, 2006.

[24] S. Mühlbauer, S. Strobl, and T. Pöschel. Isotropic stochastic rotation dynamics. *Physical Review Fluids*, 2:124204, 2017.

[25] G. Gompper, T. Ihle, D. M. Kroll, and R. G. Winkler. Multi-particle collision dynamics: A particle-based mesoscale simulation approach to the hydrodynamics of complex fluids. In C. Holm and K. Kremer, editors, *Advanced computer simulation approaches for soft matter sciences III*, volume 221 of *Advances in Polymer Science*, pages 1–87. Springer, Berlin, Heidelberg, 2009.

[26] M. Ripoll, R. G. Winkler, K. Mussawisade, and G. Gompper. Mesoscale hydrodynamics simulations of attractive rod-like colloids in shear flow. *Journal of Physics: Condensed Matter*, 20:404209, 2008.

[27] M.Yang and M. Ripoll. Thermophoretically induced flow field around a colloidal particle. *Soft Matter*, 9:4661–4671, 2013.

[28] E. Tüzel, G. Pan, T. Ihle, and D. M. Kroll. Mesoscopic model for the fluctuating hydrodynamics of binary and ternary mixtures. *Europhysics Letters*, 80:40010, 2007.

[29] E. Tüzel, G. Pan, and D. M. Kroll. Dynamics of thermally driven capillary waves for two-dimensional droplets. *Journal of Chemical Physics*, 132:174701, 2010.

[30] J. M. Haile. *Molecular Dynamics Simulation: Elementary Methods*. Wiley, New York, 1997.

[31] J. J. Brey, D. Cubero, F. Moreno, and M. J. Ruiz-Montero. Fourier state of a fluidized granular gas. *Europhysics Letters*, 53:432, 2001.

[32] G. A. Bird. The velocity distribution function within a shock wave. *Journal of Fluid Mechanics*, 30:479–487, 1967.

[33] C. Cercignani. *The Boltzmann Equation and its Applications*, volume 67 of *Applied Mathematical Sciences*. Springer, New York, 1988.

[34] G. E. Karniadakis, A. Beskok, and N. Aluru. *Microflows and Nanoflows: Fundamentals and Simulation*. Interdisciplinary Applied Mathematics. Springer, New York, 2005.

[35] T. Ihle and D. M. Kroll. Stochastic rotation dynamics: A Galilean-invariant mesoscopic model for fluid flow. *Physical Review E*, 63:020201, 2001.

[36] T. Ihle and D. M. Kroll. Stochastic rotation dynamics. I. Formalism, Galilean invariance, and Green-Kubo relations. *Physical Review E*, 67:066705, 2003.

[37] A. Donev, B. J. Alder, and A. L. Garcia. Stochastic hard-sphere dynamics for hydrodynamics of nonideal fluids. *Physical Review Letters*, 101:075902, 2008.

[38] A. Donev, B. J. Alder, and A. L. Garcia. A thermodynamically consistent non-ideal stochastic hard-sphere fluid. *Journal of Statistical Mechanics: Theory and Experiment*, 2009:P11008, 2009.

[39] A. Lamura, G. Gompper, T. Ihle, and D. M. Kroll. Multi-particle collision dynamics: Flow around a circular and a square cylinder. *Europhysics Letters*, 56:319, 2001.

[40] M. Hecht, J. Harting, T. Ihle, and H. J. Herrmann. Simulation of claylike colloids. *Physical Review E*, 72:011408, 2005.

[41] M. Hecht. *Simulation of Peloids*. PhD thesis, Universität Stuttgart, 2007.

[42] D. M. Heyes. Molecular dynamics at constant pressure and temperature. *Chemical Physics*, 82:285–301, 1983.

[43] M. P. Allen and D. J. Tildesley. *Computer Simulation of Liquids*. Clarendon Press, 1989.

[44] E. Tüzel, T. Ihle, and D. M. Kroll. Dynamic correlations in stochastic rotation dynamics. *Physical Review E*, 74:056702, 2006.

[45] T. Ihle and D. M. Kroll. Stochastic rotation dynamics. II. Transport coefficients, numerics, and long-time tails. *Physical Review E*, 67:066706, 2003.

[46] T. Ihle, E. Tüzel, and D. M. Kroll. Equilibrium calculation of transport coefficients for a fluid-particle model. *Physical Review E*, 72:046707, 2005.

[47] T. Ihle. Chapman-Enskog expansion for multi-particle collision models. *Physical Chemistry Chemical Physics*, 11:9667–9676, 2009.

[48] N. Kikuchi, C. M. Pooley, J. F. Ryder, and J. M. Yeomans. Transport coefficients of a mesoscopic fluid dynamics model. *Journal of Chemical Physics*, 119:6388–6395, 2003.

[49] C. M. Pooley and J. M. Yeomans. Kinetic theory derivation of the transport coefficients of stochastic rotation dynamics. *Journal of Physical Chemistry B*, 109:6505–6513, 2005.

[50] T. Ihle, E. Tüzel, and D. M. Kroll. Resummed Green-Kubo relations for a fluctuating fluid-particle model. *Physical Review E*, 70:035701, 2004.

[51] I. V. Pivkin and G. E. Karniadakis. A new method to impose no-slip boundary conditions in dissipative particle dynamics. *Journal of Computational Physics*, 207:114–128, 2005.

[52] D. S. Bolintineanu, J. B. Lechman, S. J. Plimpton, and G. S. Grest. No-slip boundary conditions and forced flow in multiparticle collision dynamics. *Physical Review E*, 86:066703, 2012.

[53] S. J. Cummins and M. Rudman. An SPH projection method. *Journal of Computational Physics*, 152:584–607, 1999.

[54] K. Szewc, J. Pozorski, and J.-P. Minier. Analysis of the incompressibility constraint in the smoothed particle hydrodynamics method. *International Journal for Numerical Methods in Engineering*, 92:343–369, 2012.

[55] M. Ripoll, K. Mussawisade, R. G. Winkler, and G. Gompper. Dynamic regimes of fluids simulated by multiparticle-collision dynamics. *Physical Review E*, 72:016701, 2005.

[56] A. L. Garcia and W. Wagner. Generation of the Maxwellian inflow distribution. *Journal of Computational Physics*, 217:693–708, 2006.

[57] N. A. Gatsonis, R. E. Chamberlin, and S. N. Averkin. An unstructured direct simulation Monte Carlo methodology with Kinetic-Moment inflow and outflow boundary conditions. *Journal of Computational Physics*, 233:148–174, 2013.

[58] C. Cai, I. D. Boyd, J. Fan, and G. V. Candler. Direct simulation methods for low-speed microchannel flows. *Journal of thermophysics and heat transfer*, 14:368–378, 2000.

[59] E. De Angelis, M. Chinappi, and G. Graziani. Flow simulations with multi-particle collision dynamics. *Meccanica*, 47:2069–2077, 2012.

[60] E. W. Thiele. Relation between catalytic activity and size of particle. *Industrial & Engineering Chemistry*, 31:916–920, 1939.

[61] V. Novák, P. Kočí, M. Marek, F. Štěpánek, P. Blanco-García, and G. Jones. Multi-scale modelling and measurements of diffusion through porous catalytic coatings: An application to exhaust gas oxidation. *Catalysis Today*, 188:62–69, 2012.

[62] C. Ratnasamy and J. P. Wagner. Water gas shift catalysis. *Catalysis Reviews*, 51:325–440, 2009.

[63] J. O. Hirschfelder, C. F. Curtiss, and R. B. Bird. *Molecular theory of gases and liquids*. Wiley, New York, 1954.

[64] D. F. Fairbanks and C. R. Wilke. Diffusion coefficients in multicomponent gas mixtures. *Industrial & Engineering Chemistry*, 42:471–475, 1950.

[65] J. W. Buddenberg and C. R. Wilke. Calculation of gas mixture viscosities. *Industrial & Engineering Chemistry*, 41:1345–1347, 1949.

[66] W. Wagner and H.-J. Kretzschmar. *International Steam Tables – Properties of Water and Steam based on the Industrial Formulation IAPWS-IF97*. Springer, Berlin, Heidelberg, 2008.

[67] W. Sutherland. LII. The viscosity of gases and molecular force. *The London, Edinburgh, and Dublin Philosophical Magazine and Journal of Science*, 36:507–531, 1893.

In this work, we investigate and optimize heterogeneous catalysis in porous metal foams. First, we consider the gas dynamics together with the reaction and diffusion processes in individual foam pores on the mesoscale. Second, we condense the detailed simulation results on the mesoscale to relations between few dimensionless numbers. Based on these relations, we follow a multiscale approach to derive an efficient, one-dimensional, macroscale model for metal foam filled catalytic converters. Due to its industrial relevance, we focus on the mass transfer limited regime. Finally, we develop a simple recipe to determine optimum pore size configurations. For realistic heat release values, the heat transfer out of the catalytic converter is critical. We show that, in order to keep temperature fluctuations small, the optimum configuration consists of several, stacked foam segments with decreasing pore size along the main flow direction. For typical parameters, we observe that, compared to foam with constant pore size, the trade-off between chemical conversion and flow resistance can be increased significantly, while the required reactive surface area, i.e., the needed amount of catalytic material, is reduced substantially.